Chapter 7

CONSTANT STRESS AND PRESSURE RHEOLOGY OF COLLOIDAL SUSPENSIONS: STEADY STATE BEHAVIOR AND DYNAMICS NEAR THE FLOW-ARREST TRANSITIONS

7.1 Introduction

Colloidal suspensions are ubiquitous in nature and have found widespread applications in many industrial and technological processes [1, 2]. However, our understanding in the mechanics and dynamics of *dense* suspensions remains limited. Even the simplest hard-sphere colloidal suspensions, formed by dispersing micron-sized spherical particles in a Newtonian solvent, exhibit surprisingly rich behaviors including a glass transition [3–5], yielding [6, 7], shear thinning [8, 9], and shear thickening [9–11]. These behaviors arise from Brownian motion, hydrodynamic interactions (HIs), and excluded volume effects [12]. Quantitative understanding of suspension behavior is crucial for developing novel materials, for example, "smart" materials that autonomously respond to changes in the external environment.

In this work we focus on the suspension dynamics and rheology near the flow-arrest transition, where the suspension resists continuous deformation like a solid unless the imposed stress exceeds a yield stress. The flow-arrest transition is closely related to the thermal glass transition [5] and the athermal jamming transition [13]. Their relations are succinctly summarized by the "jamming diagram" [14]: when the thermal fluctuations dominate, the suspension behavior is controlled by the glass transition, and when the flow dominates, the dynamics follow the jamming transition. Although investigations in either limit are extensive [13, 15, 16], few works are dedicated to the behavior between these limits. Moreover, considering colloidal suspensions as a model system, the implications of our work are broad, as flow-arrest transitions are also common to granular matter [17], polymer melt [18], and metallic glass [19].

Recently, we [20] discovered a universal perspective that connects the glass and jamming transitions of colloidal suspensions using constant shear stress and pressure rheology. With constant confining pressure, the suspension shear viscosity η_s and the incremental normal viscosity η_n' were found to diverge algebraically with the

volume fraction ϕ as

$$\{\eta_s, \eta_n'\} \approx \{k_s, k_n\} \times (\phi_m - \phi)^{-\alpha}, \tag{7.1}$$

where α, k_s, and k_n are constants, ϕ_m is the arrest volume fraction at the confining pressure Π, and $\alpha = 2$. Here, the incremental normal viscosity $\eta_n' = (\Pi - \Pi^{\text{eq}})/\dot{\gamma}$ with Π^{eq} the equilibrium osmotic pressure at the corresponding ϕ, and $\dot{\gamma}$ the strain rate. For weakly polydisperse suspensions, Eq. (7.1) is valid when $\phi_G \leq \phi_m \leq \phi_{\text{SAP}}$, where $\phi_G \approx 0.60$ is the glass transition volume fraction and $\phi_{\text{SAP}} \approx 0.635$ is the (protocol dependent) Shear Arrest Point (SAP) volume fraction, similar to the jamming density [20]. The only pressure dependent quantity in Eq. (7.1) is $\phi_m(\Pi)$, suggesting that the physics of jamming dominates the behavior of flow-arrest transitions, and that thermal fluctuations only play a secondary role. The key to discovering Eq. (7.1) is to hold the confining pressure constant. Indeed, were the volume, instead of the pressure, held constant, the viscosity divergence $\eta_s \sim (\phi_c - \phi)^{-\delta}$ shows different exponents δ in different limits: near the glass transition ($\phi_c = \phi_G$), the exponent $\delta \approx 2.2$–2.6 [21–24], and near the jamming transition ($\phi_c = \phi_J$), $\delta \approx 2.0$ [25–27].

However, the limitations of Ref. [20] include neglecting Hydrodynamic Interactions (HIs) in the simulations, and only addressing the basic mechanical characterization of the colloidal suspensions. We address the first limitation in the next chapter using hydrodynamic simulations. In this work we focus on the second limitation and present a comprehensive study on the suspension mechanics, structures, and diffusive dynamics that complements and extends the our earlier work [20]. The role of HIs can be revealed by comparing this chapter with the next chapter.

The second goal of this work is to investigate the granular perspective on the rheological, structural, and dynamical features of colloidal suspensions using constant shear stress and pressure rheology. Recent advances in the constitutive modeling of granular rheology highlight the importance of the granular pressure [17, 28]. In the inertial driven granular flows with particle size a and density ρ, the rheology is characterized by the inertial number $I = \dot{\gamma} a \sqrt{\rho/\Pi}$, which is the ratio of an internal time scale $a\sqrt{\rho/\Pi}$ to the flow time scale $\dot{\gamma}^{-1}$. For viscous non-Brownian suspensions, Boyer et al. [26] introduced the viscous number I_v,

$$I_v = \eta_0 \dot{\gamma}/\Pi, \tag{7.2}$$

adapting the internal time scale to η_0/Π, emphasizing the importance of viscosity.

A combination of I and I_v characterizes the flow behaviors of, for example, wet granular materials [29]

Regardless of the origin of particle interactions, the granular rheology characterizes the mechanical response using the *macroscopic* friction coefficient,

$$\mu = \sigma/\Pi, \tag{7.3}$$

i.e., the ratio of the shear stress σ to the pressure Π. This quantity remains finite as the material becomes arrested, where both Π and σ diverge. Experiments and simulations suggest that the limiting friction coefficient at arrest ($\{I, I_v\} \to 0$), μ_c, depends on the interaction details of the materials such as presence of contact friction, etc. For non-Brownian viscous suspensions, the experiments of Boyer et al. [26] show that $(\phi_c, \mu_c) = (0.585, 0.32)$. For colloidal suspensions without HIs, Wang and Brady [20] found from the μ-ϕ flow map that suspensions arrest over a yield surface from the glass transition to the non-Brownian limit at the SAP, where $(\phi_{\text{SAP}}, \mu_{\text{SAP}}) = (0.635, 0.16)$.

Although particle interactions change the arrest location, theories of dense amorphous materials [30, 31] suggest that, for non-Brownian materials, the suspension behavior away from the arrest location is less sensitive to the interactions. The incremental friction coefficient and volume fraction, $\delta\mu = \mu - \mu_c$ and $\delta\phi = \phi_c - \phi$, change as power laws of I or I_v, e.g., for dry granular materials $\delta\mu \sim I^{\alpha_\mu}$ and $\delta\phi \sim I^{\alpha_\phi}$. For example, scaling theories predict that $\alpha_\mu = \alpha_\phi = 0.35$ regardless of the particle interactions and the system dimensions [31]. The theories highlight the importance of pressure and the power of the μ-I or μ-I_v rheology in characterizing the flow behaviors of non-Brownian materials. However, the influence of thermal fluctuations are not well understood.

A key aspect in the μ-I or μ-I_v rheology of non-Brownian systems is that the pressure and the stress, instead of the volume and the strain rate, are held constant. For materials with flow-arrest transitions, specifying a stress allows the material to explore the intrinsic material response (the flowing or the arrested states) without assumptions on the macroscopic flow behaviors, and holding the pressure constant allows the material to explore the corresponding volume without assuming a maximum volume fraction [32]. This approach enabled Boyer et al. [26] to determine a critical arrest point for non-Brownian suspensions, and allowed us to construct a flow map for Brownian suspensions [20].

Another focus of the present work is the diffusive dynamics of flowing colloidal suspensions across various length scales. The most common characterization of the diffusive dynamics is the long-time self-diffusivity, which measures the diffusion on a single particle level and is extracted from the particle mean-square displacements. As ϕ increases, the self-diffusivity decreases as the particle movements are hindered by its neighbors. On the other hand, the suspension also exhibits a *collective* diffusivity, describing the collective diffusion on the length scale of suspensions in response to a weak concentration gradient [33, 34]. For dilute suspensions at equilibrium, the collective diffusivity increases with ϕ, and without HIs, is proportional to the osmotic compressibility of the suspension. Investigations on the collective diffusivity of dense suspensions are not yet available, and existing works focus on dilute systems [35, 36]. Here, we approximate the collective diffusivity by measuring the decay of the temporal correlations of the density fluctuations at vanishing wave lengths. Also, we show that the dynamic susceptibility is crucial for characterizing the collective particle motions near the flow-arrest transition [15, 37].

In constant stress and pressure rheology, when the imposed shear stress is slightly higher than the yield stress, the suspension becomes unstable and switches between flowing and arrested states. This instability provides a unique opportunity to explore the dynamic aspects of the flow-arrest transition. Here, the flow-arrest transitions are spontaneous without changing the external forcing. This is distinct from earlier start-up/cessation investigations where the stress or the flow are suddenly changed [6, 7]. Comparing to the stress fluctuations [38] with a fixed strain rate, the strain rate fluctuations are more convenient for analysis, as large stress fluctuations near the flow-arrest transitions at fixed $\dot{\gamma}$ is equivalent to fluctuations near zero strain rate with a constant σ. Spatially, the flow arrest transition often involves changes in correlation lengths both near the glass [37] and the jamming [39, 40] transitions, suggesting the emergence of cooperative particle motions. In this work, we also study the temporal and the spatial characteristic of the flow-arrest transitions.

The close connections among the suspension rheology, dynamics, and microstructures are also investigated. For example, the Stokes-Einstein-Sutherland (SES) relation states that the self-diffusivity of a single particle, d_0, is proportional to the solvent thermal fluctuations, $k_\mathrm{B}T$, and inversely proportional to the solvent viscosity η_0. The SES relation is a fluctuation-dissipation relation. Although derived from a continuum perspective involving a single particle [41], the SES relation

holds surprisingly well for the diffusion of a tagged solvent particle in equilibrium simple liquids [42], and its breakdown is often considered as a signature of the departure from the equilibrium state [43]. In non-equilibrium systems, an effective temperature is often introduced as a device to use concepts of equilibrium statistical physics [44–46]. In these systems, the choice of the effective temperature is crucial to the physical description of the system. The possibility of using an effective temperature to connect the rheology and diffusion in dense colloidal suspensions is considered in this study.

This chapter is arranged as follows: In Sec. 7.2 we describe our simulation algorithm. The general rheology, structural, and dynamical features of the constant shear stress and pressure rheology are presented in Sec. 7.3. In Sec. 7.4 we focus on both the temporal and the spatial features of suspensions near the flow-arrest transition. In Sec. 7.5, we study the behavior of flowing suspensions using a granular perspective, and model how the suspensions move away from arrested states. Sec. 7.6 connects the diffusion, rheology, and structural features, and presents the universal features using a generalized SES relation. We summarize and conclude this work in Sec. 7.7.

7.2 Simulation Method

We consider N neutrally buoyant hard-sphere particles, with radius a_i for particle i, suspended in a compressible solvent with shear viscosity η_0 and bulk viscosity κ_0, occupying a total volume V. The particle radii follow the log-normal distribution characterized by the volume averaged radius a such that $a^3 = N^{-1}\sum_{i=1}^{N} a_i^3$, and the size polydispersity defined as p.d. $= \sigma_a/\bar{a}$ with $\bar{a} = N^{-1}\sum_{i=1}^{N} a_i$ and $\sigma_a^2 = N^{-1}\sum_{i=1}^{N}(a_i^2 - \bar{a}^2)$. In the thermodynamic limit, both N and V diverge to infinity but the number density $n = N/V$ and the volume fraction $\phi = \frac{4}{3}\pi a^3 n$ remain constant. Note that, particle size polydispersity is necessary to prevent spontaneous crystallization at high density.

Without HIs, particles in the suspension follow the overdamped Langevin equation. For particle i under a linear flow characterized by the velocity gradient tensor $\mathbf{G}$, this is,

$$\zeta_i \left(\frac{\mathrm{d}\boldsymbol{x}_i}{\mathrm{d}t} - \mathbf{G} \cdot \boldsymbol{x}_i \right) = \boldsymbol{f}_i^{\mathrm{B}} + \boldsymbol{f}_i^{\mathrm{P}}, \tag{7.4}$$

where, $\boldsymbol{x}_i$ is the particle position, $\boldsymbol{f}_i^{\mathrm{P}}$ and $\boldsymbol{f}_i^{\mathrm{B}}$ are, respectively, the interparticle and the Brownian forces acting on the particle, and $\zeta_i = 6\pi\eta_0 a_i$ is the Stokes resistance for a single particle from the solvent. The velocity gradient tensor $\mathbf{G}$ is a linear combination of an isotropic extensional flow characterized by the expansion rate $\dot{e}$

and a simple shear flow characterized by the strain rate $\dot{\gamma}$, i.e.,

$$\mathbf{G} = \tfrac{1}{3}\dot{e}\mathbf{I} + \dot{\gamma}\mathbf{e}_1 \otimes \mathbf{e}_2, \tag{7.5}$$

where $\mathbf{I}$ is the idem tensor, $\otimes$ is the open product, and $\mathbf{e}_1$, $\mathbf{e}_2$, and $\mathbf{e}_3$ are respectively the unit vectors in the velocity (1), the velocity gradient (2), and the vorticity (3) directions of the simple shear flow.

The Brownian force $\boldsymbol{f}_i^{\mathrm{B}}$ satisfies the fluctuation-dissipation relation,

$$\overline{\boldsymbol{f}_i^{\mathrm{B}}} = 0 \;\text{ and }\; \overline{\boldsymbol{f}_i^{\mathrm{B}}(t)\boldsymbol{f}_i^{\mathrm{B}}(0)} = 2k_{\mathrm{B}}T\zeta\mathbf{I}\delta(t), \tag{7.6}$$

where $\delta(x)$ is the Dirac delta function, and $k_{\mathrm{B}}T$ is the thermal energy scale. The interparticle force is computed pairwise as

$$\boldsymbol{f}_i^{\mathrm{P}} = \sum_{j=1}^{N} \boldsymbol{f}_{ij}^{\mathrm{P}}, \tag{7.7}$$

where the force from particle j on particle i, $\boldsymbol{f}_{ij}^{\mathrm{P}} = -\partial V_{ij}/\partial \boldsymbol{x}_i$, with the hard-sphere potential $V_{ij} = H(a_i + a_j - r_{ij})$. Here, $r_{ij} = \|\boldsymbol{x}_i - \boldsymbol{x}_j\|$ and $H(x)$ is the Heaviside function. Note that for a hard-sphere potential, $\boldsymbol{f}_i^{\mathrm{P}}$ diverges at particle contact, and is zero everywhere else. Moreover, we impose periodic boundary condition in the 1- and 3-directions and the Lees-Edwards boundary condition in the 2-direction. The simulation box size L is also adjusted isotropically based on $\dot{e}$ as $\mathrm{d}L/\mathrm{d}t = \frac{1}{3}\dot{e}L$.

To impose the constant stress and pressure constraints on the suspension, we consider the macroscopic stress balance on the suspension. Without HIs, the bulk stress of a suspension with compressible solvent is [47],

$$\langle\boldsymbol{\Sigma}\rangle = (\kappa_0 + \tfrac{4}{3}\eta_0\phi)(\mathbf{G} : \mathbf{I})\mathbf{I} + 2\eta_0(1 + \tfrac{5}{2}\phi)\mathbf{E} + \boldsymbol{\sigma}^{\mathrm{P}}, \tag{7.8}$$

where the rate of strain tensor $\mathbf{E} = \frac{1}{2}(\mathbf{G} + \mathbf{G}^{\dagger}) - \frac{1}{3}(\mathbf{G} : \mathbf{I})\mathbf{I}$, where $\dagger$ is the transpose, and the stress due to particle interactions,

$$\boldsymbol{\sigma}^{\mathrm{P}} = -nk_{\mathrm{B}}T\mathbf{I} - n\left\langle \boldsymbol{x}\boldsymbol{f}^{\mathrm{P}} \right\rangle, \tag{7.9}$$

containing contributions from thermal fluctuations and the spacial moment of interparticle forces [48], i.e., $n\left\langle \boldsymbol{x}\boldsymbol{f}^{\mathrm{P}} \right\rangle = V^{-1}\sum_{i=1}^{N} \boldsymbol{x}_i\boldsymbol{f}_i^{\mathrm{P}}$. Note that $\boldsymbol{\sigma}^{\mathrm{P}}$ depends only on the instantaneous particle configuration due to the overdamped suspension dynamics. Therefore, one can specify the imposed shear stress $\sigma = \langle\boldsymbol{\Sigma}\rangle : (\mathbf{e}_1 \otimes \mathbf{e}_2)$ and the imposed pressure $\Pi = -\frac{1}{3}\langle\boldsymbol{\Sigma}\rangle : \mathbf{I}$ and solve for $\dot{\gamma}$ and $\dot{e}$ according to Eq. (7.8):

$$\sigma = (1 + \tfrac{5}{2}\phi)\eta_0\dot{\gamma} + \boldsymbol{\sigma}^{\mathrm{P}} : (\mathbf{e}_1 \otimes \mathbf{e}_2), \tag{7.10}$$

$$\Pi = -(\kappa_0 + \tfrac{4}{3}\phi\eta_0)\dot{e} - \tfrac{1}{3}\boldsymbol{\sigma}^{\mathrm{P}} : \mathbf{I}, \tag{7.11}$$

assuming that the imposed linear flow can be described by $\mathbf{G}$ in Eq. (7.5). In addition, Eq. (7.11) shows that a compressible solvent with bulk viscosity κ_0 allows isotropic compression to be imposed without violating the physics of Brownian particles in Stokes flow, and avoids using physical permeable boundaries which may cause complications such as local ordering. This is indeed the novelty of our method: through a compressible solvent, the constant pressure constraint is satisfied without introducing boundaries.

In Brownian dynamics (BD) simulations, Eq. (7.4) is integrated with respect to time. To resolve the singular hard-sphere potential, we adopt the "potential-free" algorithm [49–52]. In this method, the interparticle force and the non-overlapping conditions are maintained in a predictor-corrector fashion: at time t, the particle configuration is first progressed according to Eq. (7.4) without considering $\boldsymbol{f}_i^{\mathrm{P}}$ to $t + \Delta t$. In the corrector step, the algorithm checks particle overlap and moves the overlapping particles back to contact pairwise along the line that connects the particle centers until the suspension is overlap-free. Specifically, if $r_{ij} < (a_i + a_j)$ for particles i at j, the particles are moved along $(\boldsymbol{x}_i - \boldsymbol{x}_j)$ according to

$$\Delta\boldsymbol{x}_i = a_j\boldsymbol{\Delta}_{ij} \text{ and } \Delta\boldsymbol{x}_j = -a_i\boldsymbol{\Delta}_{ij}, \tag{7.12}$$

where $\boldsymbol{\Delta}_{ij} = (\boldsymbol{x}_i - \boldsymbol{x}_j)[r_{ij}^{-1} - (a_i + a_j)^{-1}]$. The interparticle force for the pair is calculated based on the Stokes relation,

$$\boldsymbol{f}_{ij}^{\mathrm{P}} = \zeta_i\Delta\boldsymbol{x}_i/\Delta t. \tag{7.13}$$

Here, the Newton's third law, $\boldsymbol{f}_{ij}^{\mathrm{P}} + \boldsymbol{f}_{ji}^{\mathrm{P}} = 0$, is satisfied. Despite its simplicity, the potential-free algorithm has been extensively used to investigate systems with hard-sphere interactions such as start-up [6, 53] and oscillatory [54] bulk rheology, steady and transient microrheology [55, 56], osmotic propulsion [57], and active materials [58]. It has also been used to validate studies in dilute [59] and dense [60] suspensions, and compares favorably with molecular dynamics simulations [61].

Using the above algorithm, we perform constant shear stress and pressure rheology simulations with imposed shear stress σ and imposed pressure Π. Scaling σ and Π with the thermal energy $k_{\mathrm{B}}T$ leads to two key simulation parameters, the stress Péclet number Pe_σ and the scaled pressure $\bar{\Pi}$, defined as

$$\mathrm{Pe}_\sigma = \frac{6\pi a^3\sigma}{k_{\mathrm{B}}T} \text{ and } \bar{\Pi} = \frac{a^3\Pi}{k_{\mathrm{B}}T}. \tag{7.14}$$

As pointed out by Swan and Brady [62], Pe_σ is trivially connected to the strain rate Péclet number $\mathrm{Pe}_{\dot\gamma} = 6\pi a^3\eta_0\dot\gamma/(k_\mathrm{B}T)$ through

$$\mathrm{Pe}_{\dot\gamma} = (\eta_0/\eta_s)\mathrm{Pe}_\sigma, \tag{7.15}$$

where $\eta_s = \sigma/\dot\gamma$ is the suspension shear viscosity. The simulation time is scaled with a^2/d_0, with the Stokes-Einstein-Sutherland diffusivity $d_0 = k_\mathrm{B}T/(6\pi\eta_0 a)$, when $\mathrm{Pe}_\sigma \le 1$, and with η_0/σ when $\mathrm{Pe}_\sigma > 1$. The stress-scaled time automatically adjusts the resolution of configuration evolution with respect to the strain rate $\dot\gamma$. That is, because the dimensionless time step $\Delta\tau = \sigma\Delta t/\eta_0 = \dot\gamma\Delta t(\eta_s/\eta_0)$, for a fixed $\Delta\tau$, the higher the suspension shear viscosity, the smaller the dimensionless time step with respect to strain rate, $\dot\gamma\Delta t$. Therefore, with a fixed $\Delta\tau$, the constant stress and pressure rheology improves the temporal resolution of the configuration evolution for suspensions with large η_s.

We explore a wide range of Π and σ combinations to map out the flow behaviors using dynamic simulations. Each simulation contains $N = 200$ particles with a particle size polydispersity p.d. $= 0.1$. For convenience, the number of particle species with different radii is limited to 20. Increasing N does not qualitatively alter the results. A simulation begins with an random, non-overlapping polydisperse hard-sphere configuration generated by a modified Lubachesvky-Stillinger algorithm [63, 64] at an estimated starting volume fraction ϕ_0, and lasts for 5000 dimensionless time with a step size 10^{-3}. When computing the results, the first 1000 time units are discarded. In this work, the suspension is considered flowing when the shear viscosity $\eta_s < 2000$, and such that the suspensions have flown at least 2 strains. Moreover, the solvent bulk viscosity κ_0 affects how the suspension respond to the imposed pressure by controlling the rate at which the simulation cell changes its volume. If κ_0 is too large, the suspension cannot reach the steady state volume fraction by the end of the simulation, and if κ_0 is too small, the suspension may experience large density fluctuations. Once reaching the steady state, the suspension rheology becomes independent of κ_0. We found that with $\kappa_0/\eta_0 = 2000$, the suspensions can reach the steady state sufficiently fast for low $\bar\Pi$ without becoming unstable at high $\bar\Pi$. The volume control mechanism is slightly different from Ref. [20], where the bulk viscosity that controls the cell volume changes depends on the instantaneous volume fraction ϕ. Furthermore, for each (Π, σ) pair, we perform at least three independent runs to eliminate the dependence on initial configurations.

To validate the simulation method, Fig. 7.1 presents the osmotic pressure Π for polydisperse suspensions with p.d. $= 0.1$ as a function of ϕ using constant pressure

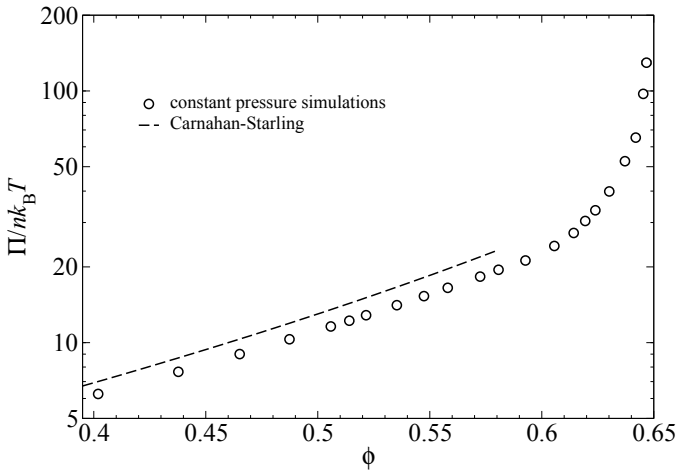

Figure 7.1: The suspension equilibrium osmotic pressure $\Pi/(nk_BT)$ as a function of the volume fraction ϕ, computed using constant pressure Brownian Dynamics simulations. The suspension size polydispersity p.d. = 0.1. The dashed line is the osmotic pressure from Carnahan-Starling equation of state for monodisperse suspensions. The error in ϕ is smaller than the symbol size.

simulations with $\dot{\gamma} = 0$. The error in ϕ is smaller than the symbol size even at the highest imposed pressure. Fig. 7.1 also shows, in dashed line, the Carnahan-Starling (CS) equation of state for monodisperse suspensions,

$$\frac{\Pi}{nk_BT} = \frac{1 + \phi + \phi^2 - \phi^3}{(1-\phi)^3}, \tag{7.16}$$

valid up to $\phi \approx 0.49$. The osmotic pressure diverges near $\phi \approx 0.65$. The particle size polydispersity effectively disrupts the spontaneous crystallization, evidenced by the continuous pressure increase with respect to ϕ and by the suspension microstructures. The size polydispersity also reduces the osmotic pressure comparing to the monodisperse systems, and increases the jamming volume fraction where the pressure diverges.

7.3 General features of flowing suspensions

Shear viscosity and volume fraction

The principle outputs of the constant stress and pressure simulations are the suspension strain rate $\dot{\gamma}$ and the volume fraction ϕ. At each time step, the instantaneous strain rate $\dot{\gamma}$ is from solving Eq. (7.10), and the instantaneous volume fraction ϕ is from monitoring the size of the simulation cell L. Fig. 7.2a presents the Pe_σ dependence of the steady state shear viscosity η_s and normal viscosity η_n for flowing

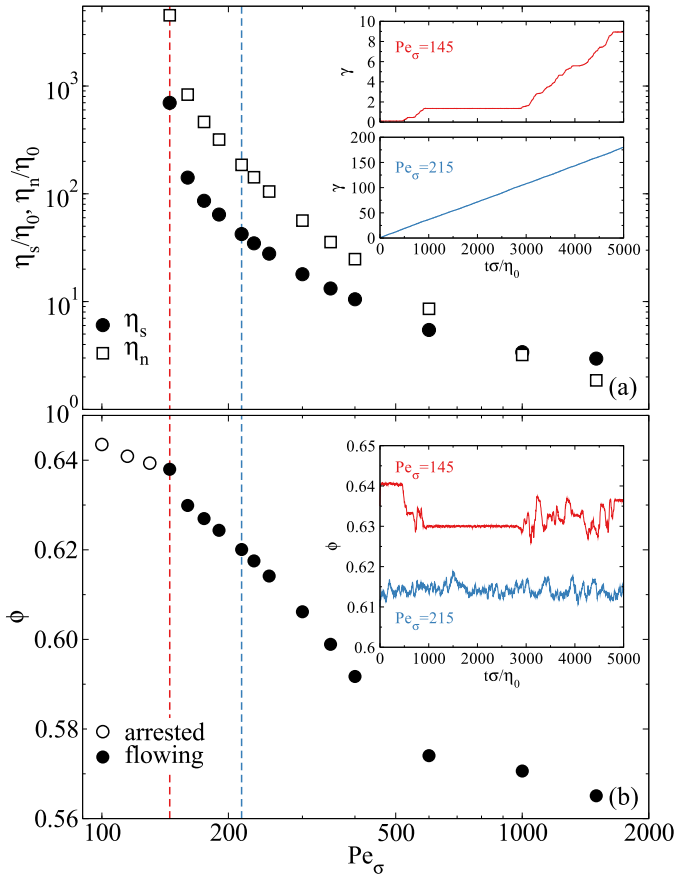

Figure 7.2: (Color online) Simulation results as functions of the stress Péclet number $\mathrm{Pe}_\sigma = 6\pi\sigma a^3/k_\mathrm{B}T$ at an imposed pressure $\bar{\Pi} = \Pi a^3/k_\mathrm{B}T = 50$. (a): the shear and the normal viscosities, η_s and η_n, respectively, and (b): the volume fraction ϕ. In (b), the arrested results are shown as open symbol. The insets of (a) show the time evolution of the accumulated strain γ at $\mathrm{Pe}_\sigma = 145$ and 215. The inset of (b) presents the corresponding time evolution of ϕ at the same Péclet numbers.

suspensions at an imposed pressure $\bar{\Pi} = 50$. Here, the normal viscosity,

$$\eta_n = \Pi/\dot{\gamma}, \tag{7.17}$$

accounts for the effect of the flow on the suspension pressure. At this imposed pressure, the suspension exhibits a yield stress, and is only able to flow when the stress Péclet number $\mathrm{Pe}_\sigma \geq 145$. For flowing suspensions, both η_s and η_n reduce several orders of magnitude with increasing Pe_σ from 145 to 10^3. The normal viscosity η_n is higher than the shear viscosity η_s when $\mathrm{Pe}_\sigma < 10^3$, and becomes lower afterwards as η_s approaches the solvent viscosity η_0 as $\mathrm{Pe}_\sigma \to \infty$, but η_n does not have a limiting value at high Pe_σ. Clearly, with a finite $\bar{\Pi}$, in the high

Pe_σ limit the particle interaction contributes negligibly to η_s due to dilation. If the volume fraction ϕ were fixed, the pressure $\Pi \sim \eta_0\dot{\gamma}$ as $\mathrm{Pe}_\sigma \to \infty$, and with fixed $\bar{\Pi} = \Pi a^3/k_\mathrm{B}T$, $\Pi \sim k_\mathrm{B}T$. Therefore, to keep $\bar{\Pi}$ constant with increasing Pe_σ, suspension dilation, i.e., a decrease in ϕ, is necessary, leading to vanishing particle viscosity contribution. Therefore, in the $\mathrm{Pe}_\sigma \to \infty$ limit, the confining pressure is too weak to "confine" the suspension. This is different from the constant volume hard-sphere suspension rheology [51], where the particle interactions' contribution to η_s is finite as $\mathrm{Pe}_\sigma \to \infty$, due to the formation of a particle accumulation boundary layer near contact [65].

The insets of Fig. 7.2a show the time evolution of the accumulated strain $\gamma(t) = \int_0^t \dot{\gamma}(\tau)\mathrm{d}\tau$ at $\mathrm{Pe}_\sigma = 145$ and 215. At $\mathrm{Pe}_\sigma = 215$, the suspension flows, and γ grows linearly with $t\sigma/\eta_0$, suggesting that the suspension flows continuously. The slope of the γ-t curve is inversely proportional to η_s. Close to the flow-arrest transition at $\mathrm{Pe}_\sigma = 145$, however, the accumulated strain does not grow linearly with time and is unstable: the suspension can become arrested before flowing again. These insets illustrates how the flow-arrest transitions can profoundly affect the suspension dynamics. In Sec. 7.4, we further study the suspension dynamics near the flow-arrest transitions.

Fig. 7.2b shows the average suspension volume fraction ϕ as a function of Pe_σ. Here, the arrested states are shown in open circles and the flowing states in filled circles. The suspension dilates (decreasing ϕ) with increasing Pe_σ both in the flowing and the arrested states. Not shown in this figure is that at even lower Pe_σ, ϕ approaches a constant zero-flow value. That ϕ decreases with increasing Pe_σ in both the arrested and the flowing states suggests that dilation precedes flowing in constant stress and pressure rheology, as the onset of flow requires more space among neighboring particles. For flowing suspensions, the strong shear thinning in η_s and η_n is consistent with the reduction in ϕ. Furthermore, when $\mathrm{Pe}_\sigma \gtrsim 500$, ϕ decreases much slower with growing Pe_σ compared to the case at lower Pe_σ, suggesting that the suspension undergoes qualitative changes, which are revealed in Fig. 7.3 as the formation of string-phase structures. However, such changes are not visible in the viscosity results of Fig. 7.2a.

The inset of Fig. 7.2b shows the time evolution of ϕ, also at $\mathrm{Pe}_\sigma = 145$ and 215. For flowing suspensions at $\mathrm{Pe}_\sigma = 215$, the volume fraction fluctuates with time about its mean value. Near the flow arrest transition ($\mathrm{Pe}_\sigma = 145$), similarly to γ in Fig. 7.2a, ϕ is also unstable. In this case, when the suspension is flowing (γ

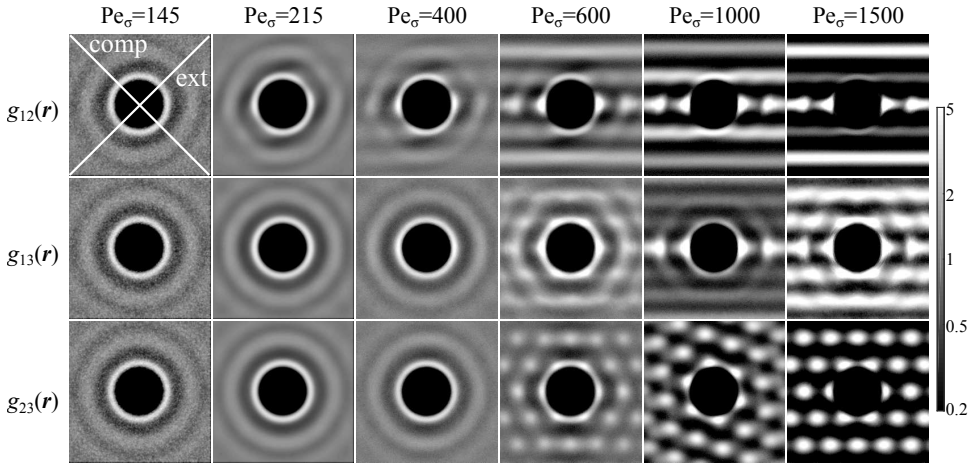

Figure 7.3: Equatorial slices of pair distribution function in the velocity-velocity gradient $g_{12}(\boldsymbol{r})$, velocity-vorticity $g_{13}(\boldsymbol{r})$, and velocity gradient-vorticity $g_{23}(\boldsymbol{r})$ planes at various Pe_σ with an imposed pressure $\bar{\Pi} = 50$. The slice width is $0.7a$. On the panel for $g_{12}(\boldsymbol{r})$ at $\mathrm{Pe}_\sigma = 145$ the compressional and the extensional axis are also highlighted.

increases with time), the corresponding ϕ exhibits more fluctuations compared to arrested suspensions. The volume fractions corresponding to the arrested states are not necessarily higher than the flowing states. This suggests that the suspension structure, not the volume fraction, is the deciding factor in the flow behaviors.

Real- and wave-space structural features

Next we examine the suspension microstructures. A common real-space structural characterization is the pair distribution function

$$g(\boldsymbol{r}) = \frac{V}{N^2}\left\langle \sum_{i,j}{}' \delta(\boldsymbol{r} - \boldsymbol{x}_i + \boldsymbol{x}_j)\right\rangle, \tag{7.18}$$

where the prime on the summation excludes the case of $i = j$. Fig. 7.3 presents the equatorial slices of $g(\boldsymbol{r})$ in the velocity-velocity gradient (12-), velocity-vorticity (13-), and velocity gradient-vorticity (23-) planes with a width of $0.7a$ at various Pe_σ and $\bar{\Pi} = 50$. Also shown in Fig. 7.3 are the compressional and the extensional axis in the shear plane.

The most striking feature of Fig. 7.3 is the formation of a "string phase" in suspensions when $\mathrm{Pe}_\sigma \geq 600$. This is evidenced by the lines in the velocity direction in $g_{12}(\boldsymbol{r})$ and $g_{13}(\boldsymbol{r})$, and nearly hexagonal crystalline structures in $g_{23}(\boldsymbol{r})$. The orientation of the hexagonal structures in $g_{23}(\boldsymbol{r})$ can shift with different simulations. Although the particle size polydispersity effectively disrupts the suspension crystal-

lization at low Pe_σ, it does not prevent the string phase formation at higher Pe_σ. The string phase also persists with increasing Pe_σ because HIs are absent. As is shown in the next chapter, HIs lead to a reentrant of amorphous structures at higher Pe_σ.

The suspension structure remains homogeneous when $\mathrm{Pe}_\sigma < 600$. In the shear plane, $g_{12}(\boldsymbol{r})$ exhibits increasing distortion towards the extensional axis with increasing Pe_σ. At $\mathrm{Pe}_\sigma = 400$, the homogeneous structural distortion is the most pronounced in Fig. 7.3. For two nearby particles in the shear flow, they are most likely to form a pair of close contact in the velocity direction, shown by the high probability of $g_{12}(\boldsymbol{r})$. The pair rotates from the compressional quadrant towards the extensional quadrant, and then disengages near the extensional axis. Meanwhile, at this Pe_σ, the structures of $g_{13}(\boldsymbol{r})$ and $g_{23}(\boldsymbol{r})$ remain isotropic. Note that the structural distortion in $g_{12}(\boldsymbol{r})$ is not apparent until $\mathrm{Pe}_\sigma = 215$, where the suspension flows appreciably.

The structural distortion shown in Fig. 7.3 is intimately related to the suspension rheology. For monodisperse systems without HIs, the structural distortion contributes to the suspension stress as [51, 66]:

$$n\left\langle \boldsymbol{x}\boldsymbol{f}^{\mathrm{P}}\right\rangle + \Pi^{\mathrm{eq}}\mathbf{I} = \frac{27}{2\pi}\eta_0\dot{\gamma}\phi^2\frac{g^{\mathrm{eq}}(2)}{\hat{d}}\int \hat{\boldsymbol{r}}\hat{\boldsymbol{r}}\hat{f}(2;\Omega)\mathrm{d}\Omega, \tag{7.19}$$

where Ω is the solid angle, and the suspension structure is decomposed to an equilibrium contribution $g^{\mathrm{eq}}(\boldsymbol{r})$ and a flow contribution $\hat{f}(\boldsymbol{r})$ as $g(\boldsymbol{r}) = g^{\mathrm{eq}}(\boldsymbol{r})[1 + (\mathrm{Pe}_{\dot{\gamma}}/\hat{d})\hat{f}(\boldsymbol{r})]$, where $\hat{d}$ is a characteristic diffusion scale describing the suspension relaxation process. With an appropriate choice of $\hat{d}$, the suspension rheology entirely depends on the structural distortion $\hat{f}$. In the constant ϕ study of Foss and Brady [51], the structural distortion $\hat{f}$ contribute positively to the shear viscosity, leading to a viscosity decrease slower than a $\mathrm{Pe}_{\dot{\gamma}}^{-1}$ decay.

From Eq. (7.19), the structural distortion in the compressional and the extensional axis contributes most significantly to the shear viscosity. Fig. 7.4 presents the peak values of $g(\boldsymbol{r})$ in these two axis, $\max(g_{\mathrm{comp}})$ and $\max(g_{\mathrm{ext}})$, as functions of Pe_σ at the same imposed pressure of $\bar{\Pi} = 50$. Note that, due to symmetry, both the accumulation in the compressional axis and the depletion in the extensional axis contribute positively to Eq. (7.19) [6], and therefore, the difference $\max(g_{\mathrm{comp}}) - \max(g_{\mathrm{ext}})$ qualitatively captures the structural contributions to the suspension viscosity.

Comparing to Fig. 7.3, the most distinguishing feature in Fig. 7.4 is that the behaviors in $\max(g_{\mathrm{comp}})$ and $\max(g_{\mathrm{ext}})$ are qualitatively different between the homogeneous and the string phase suspensions, which occurs around $\mathrm{Pe}_\sigma = 500$. With $\mathrm{Pe}_\sigma < 500$,

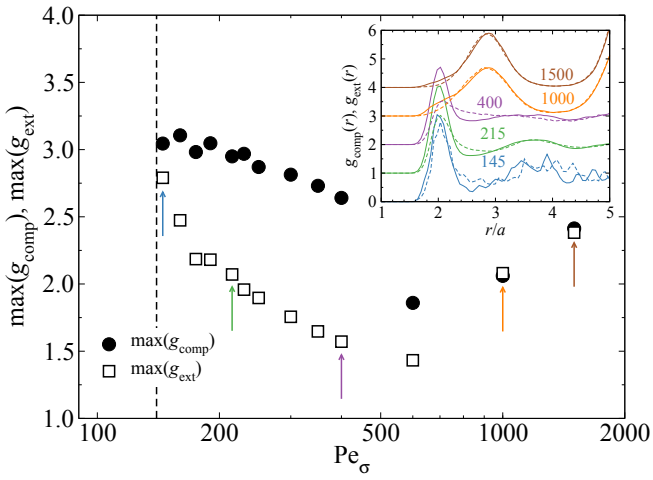

Figure 7.4: (Color online) The peak values of the pair distribution function in the compressional and the extensional axes, $\max(g_{\text{comp}})$ and $\max(g_{\text{ext}})$ as functions of Pe_σ at the imposed pressure $\bar{\Pi} = 50$. The vertical dashed line represents the estimated yield Pe_σ beyond which the suspension begins to flow. The inset presents the radial variation of $g_{\text{comp}}(r)$ (solid line) and $g_{\text{ext}}(r)$ (dashed line) at various Pe_σ, which are also pointed out by arrows in the main figure with their corresponding color. The curves are shifted for clarity when $\text{Pe}_\sigma \geq 215$.

both $\max(g_{\text{comp}})$ and $\max(g_{\text{ext}})$ decrease with increasing Pe_σ due to suspension dilation. With fixed volume, $\max(g_{\text{comp}})$ is expected to increase with increasing Péclet number [6]. The difference, $\max(g_{\text{comp}}) - \max(g_{\text{ext}})$, increases with Pe_σ, suggesting that the suspension structure becomes increasingly distorted. On the other hand, for $\text{Pe}_\sigma > 500$, both $\max(g_{\text{comp}})$ and $\max(g_{\text{ext}})$ grow with Pe_σ, and their difference disappears when $\text{Pe}_\sigma \geq 1000$ due to the formation of aligned string structures in the suspension.

The inset of Fig. 7.4 shows the $g_{\text{comp}}(r)$ in solid lines and $g_{\text{ext}}(r)$ in dashed lines at different Pe_σ; the results for $\text{Pe}_\sigma \geq 215$ are shifted for clarity. For $\text{Pe}_\sigma = 1000$ and 1500, the difference between $g_{\text{comp}}(r)$ and $g_{\text{ext}}(r)$ is almost indistinguishable due to the formation of the string phase. On the other hand, for homogeneous suspensions, the difference between $g_{\text{comp}}(r)$ and $g_{\text{ext}}(r)$ grows with increasing Pe_σ. With increasing Pe_σ, the first peaks in $g_{\text{comp}}(r)$ and $g_{\text{ext}}(r)$ become narrower, and the features beyond the first peak vanish, i.e., the distribution functions at $\text{Pe}_\sigma = 145$ show more pronounced undulations beyond the first peaks compared to those at $\text{Pe}_\sigma = 400$. Evidently, the microstructures of the homogeneous suspension are distinctly different from those of the string phase.

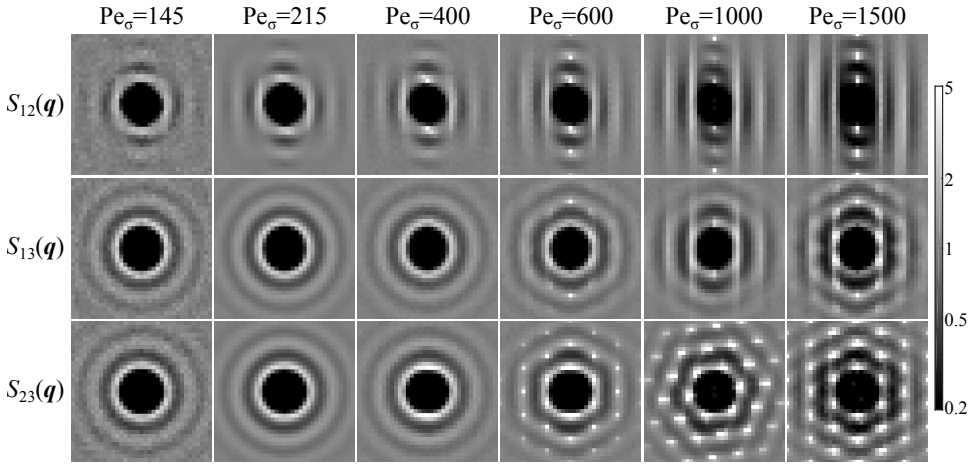

Figure 7.5: The static structure factors $S_{12}(\boldsymbol{q})$, $S_{13}(\boldsymbol{q})$, and $S_{23}(\boldsymbol{q})$ at various Pe_σ with an imposed pressure $\bar{\Pi} = 50$. Each panel depicts the structure factor $S(\boldsymbol{q})$ in the wave space from $-10qa$ to $10qa$ in both directions.

Complementary to real-space characterizations such as the pair-distribution function $g(\boldsymbol{r})$, the suspension structures are also frequently assessed via wave-space characterizations such as the static structure factor $S(\boldsymbol{q})$ [67, 68]. Defining the instantaneous wave-space density fluctuations [69],

$$n_{\boldsymbol{q}}(t) = \frac{1}{\sqrt{N}} \sum_{i=1}^{N} \exp[i\boldsymbol{q} \cdot \boldsymbol{x}_i(t)], \tag{7.20}$$

where $\boldsymbol{q}$ is the wave vector, the static structure factor is the instantaneous correlation, defined as

$$S(\boldsymbol{q}) = \left\langle n_{\boldsymbol{q}}(0) n_{-\boldsymbol{q}}(0) \right\rangle. \tag{7.21}$$

Fig. 7.5 presents the 2D static structure factors $S(\boldsymbol{q})$ in different wave-space planes. Here, the fundamental lattice vectors for the periodic simulation box corresponding to the 1-, 2-, and 3-directions are respectively $\mathbf{b}_1$, $\mathbf{b}_2$, and $\mathbf{b}_3$, and the wave vectors in, for example, $S_{12}(\boldsymbol{q})$, are $\boldsymbol{q} = i\mathbf{b}_1 + j\mathbf{b}_2$ with integers i and j. The wave-number in each direction in Fig. 7.5 is limited from $-10qa$ to $10qa$. In simulations with periodic boundary conditions, the maximum wave-space resolution is $2\pi/L$, strongly affected by the system size.

The structural information from $S(\boldsymbol{q})$ in Fig. 7.5 is consistent with the $g(\boldsymbol{r})$ characterizations in Fig. 7.3. In fact, $S(\boldsymbol{q})$ strongly resembles the $g(\boldsymbol{r})$ slices rotated counterclockwise by 90°. The wave-space characterization confirms the string phase formation with $\mathrm{Pe}_\sigma \geq 600$, which is especially evident with the regular hexagonal patterns in $S_{23}(\boldsymbol{q})$, and otherwise homogeneous suspension structures at lower Pe_σ.

In addition, the wave-space characterization is more sensitive to structural distortions, i.e., at $\mathrm{Pe}_\sigma = 145$, the structural distortion is already evident in $S_{12}(\boldsymbol{q})$, but appears isotropic in $g_{12}(\boldsymbol{r})$. Moreover, at $\mathrm{Pe}_\sigma = 400$, $S_{23}(\boldsymbol{q})$ distorts towards the velocity gradient direction, suggesting stronger structural correlations, which is not captured in $g_{23}(\boldsymbol{r})$. Otherwise, $S_{23}(\boldsymbol{q})$ and $S_{13}(\boldsymbol{q})$ are isotropic for homogeneous suspensions.

Suspension diffusion

Fig. 7.6 presents various dynamic characterization of suspensions as functions of Pe_σ at $\bar{\Pi} = 50$. The estimated flow-arrest boundary is shown as dash-dotted line. Fig. 7.6a shows the long-time self-diffusivity in the velocity gradient direction, $d^s_{\infty,22}$ (open symbols), and the vorticity direction, $d^s_{\infty,33}$ (filled symbols). In the k-direction, the long-time self-diffusivity is defined as

$$d^s_{\infty,kk} = \frac{1}{2}\lim_{t\to\infty}\frac{\mathrm{d}}{\mathrm{d}t}\left\langle \Delta x_k^2 \right\rangle, \tag{7.22}$$

where $\left\langle \Delta x_k^2 \right\rangle$ is the k-direction mean-square displacement averaged over all available times of particle trajectories. The mean-square displacements $\left\langle \Delta x_2^2 \right\rangle$ (dashed line) and $\left\langle \Delta x_3^2 \right\rangle$ (solid line) at selected Pe_σ are shown in the inset of Fig. 7.6a. The corresponding Pe_σ for flowing suspensions are are pointed out by arrows in the main figure, and a dash-dotted line is present at $\mathrm{Pe}_\sigma = 115$ for the arrested suspension.

In Fig. 7.6a, the scaled diffusivity $d^s_{\infty,33}/d_0$ emerges from a infinitesimal value as the imposed stress exceeds the yield stress to cause the suspension to flow, suggesting that the particle inherent thermal fluctuations contribute little to the dynamics. After the suspension begins to flow, further increasing Pe_σ also increases $d^s_{\infty,33}/d_0$ as the flow drives the particle diffusion. The increase in the diffusivity is significant, partly due to the suspension dilation. When the suspension forms a string phase at $\mathrm{Pe}_\sigma > 500$, the diffusivity stops to grow and decreases with increasing Pe_σ, as the string structure limits the diffusive movements. The diffusivity in the velocity gradient direction $d^s_{\infty,22}/d_0$ is consistent with its vorticity direction counterpart except for small quantitative differences. When the suspension is amorphous $\mathrm{Pe}_\sigma < 500$, $d^s_{\infty,22} > d^s_{\infty,33}$ due to the linear shear flow, and in the string phase, $d^s_{\infty,33} > d^s_{\infty,22}$.

The inset of Fig. 7.6a shows the time evolution of the mean-square displacement up to a diffusive time of $2a^2/d_0$. Within this time frame, at $\mathrm{Pe}_\sigma = 115$, the suspension is arrested, and the particles are confined to the cage formed by their neighbors. However, at $\mathrm{Pe}_\sigma = 145$, the suspension becomes flowing and the

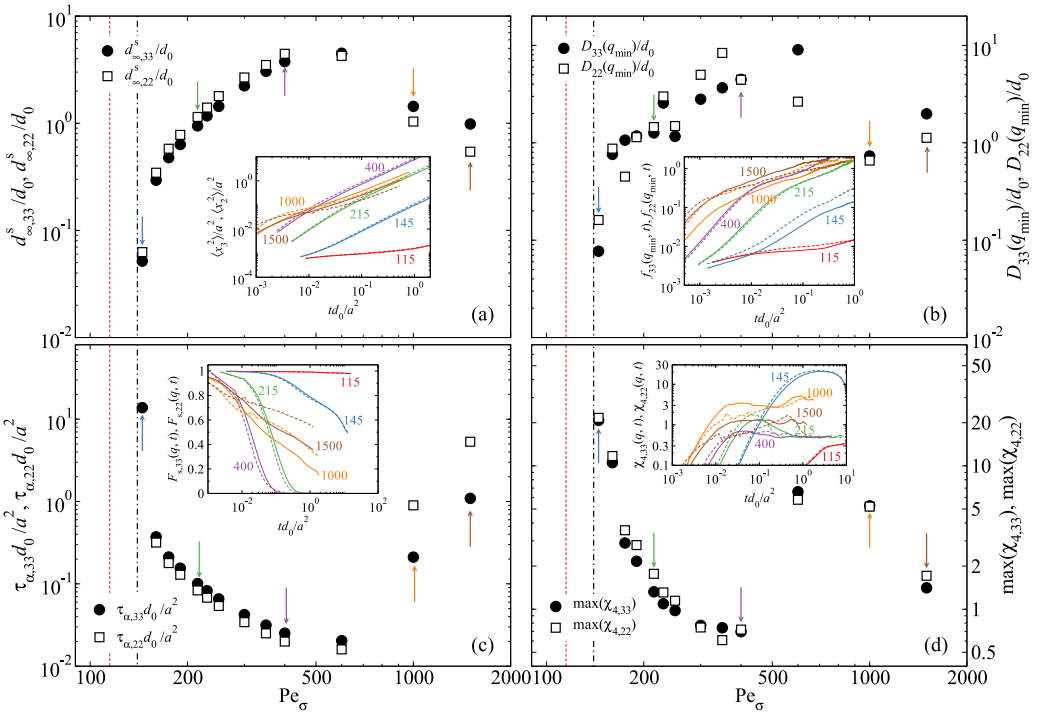

Figure 7.6: (Color online) Diffusive dynamics of suspensions as functions of Pe_σ at $\bar{\Pi} = 50$. The dash-dotted vertical lines represent the estimated arrest Pe_σ. The measurements in the vorticity direction, denoted by subscript 33, are shown as filled symbols in the main figures and solid lines in the insets. In the velocity gradient direction, denoted by subscript 22, the results are shown as open symbols and dashed lines. (a): The scaled long-time self-diffusivities, $d^s_{\infty,33}/d_0$ and $d^s_{\infty,22}/d_0$. The inset shows the time evolution of the mean-square displacement in the 3- and 2-directions, $\langle x_3^2 \rangle$ and $\langle x_2^2 \rangle$, at various Pe_σ, which are highlighted by arrows for flowing suspensions, and by vertical dashed lines for arrested suspensions in corresponding colors. (b): The scaled wave-number dependent diffusivities, $D_{33}(q_{\min})/d_0$ and $D_{22}(q_{\min})/d_0$, where $q_{\min}$ is the smallest measurable wave number in the unit cell. The inset shows the time evolution of the functions $f_{33}(q,t)$ and $f_{22}(q,t)$ defined in Eq. (7.25) at various Pe_σ. (c): The scaled α-relaxation times, $\tau_{\alpha,33}d_0/a^2$ and $\tau_{\alpha,22}d_0/a^2$, measured from the decay of the self-intermediate scattering function $F_s(q,t)$ at $qa = 3.5$. The inset shows the time evolution of the corresponding $F_s(q,t)$ in different directions at various Pe_σ. (d): The maximum of the dynamic susceptibilities, max($\chi_{4,33}$) and max($\chi_{4,22}$), measured at wave number $qa = 3.5$ in different directions. The inset shows the time evolution of the corresponding dynamic susceptibilities $\chi_{4,\alpha\alpha}(q,t)$ in different directions at various Pe_σ.

particle movement becomes diffusive, characterized by the linear growth of the mean-square displacement at large times. Increasing Pe_σ also changes the transition to the long-time diffusive behavior. At $\mathrm{Pe}_\sigma = 145$, the particle becomes diffusive

from a subdiffusive regime, consistent with the cage-breaking process in sheared suspensions. On the other hand, at $\mathrm{Pe}_\sigma = 215$ and 400, before entering long-time diffusive regime, the suspension is superdiffusive, i.e., $\left\langle \Delta x^2 \right\rangle \propto t^2$, suggesting that diffusion arises from strong particle interactions. Finally, in the string phase ($\mathrm{Pe}_\sigma =$ 1000 and 1500), the particles enter a sub-diffusive regime from the superdiffusive behavior before becoming diffusive. This is because the structural formation hinders the diffusion process, leading to much lower diffusivities in Fig. 7.6a. For amorphous suspensions, the difference between the 2- and 3- directions is small, but with string formation, the difference becomes more significant.

Another characterization of the suspension diffusive behavior is the wave-number dependent diffusivity $\boldsymbol{D}(\boldsymbol{q})$ which characterize the suspension diffusion over different length scales. From a small-wave length expansion of the Smoluchowski equation which describes the suspension dynamics [35, 36], it can be shown that in directions perpendicular to the 1-direction, the time-dependent structure factor,

$$S(\boldsymbol{q}, t) = \left\langle n_{\boldsymbol{q}}(t) n_{-\boldsymbol{q}}(0) \right\rangle, \tag{7.23}$$

decays as

$$S(\boldsymbol{q}, t) = S(\boldsymbol{q}) \exp[-\boldsymbol{q} \cdot \boldsymbol{D}(\boldsymbol{q}) \cdot \boldsymbol{q} t], \tag{7.24}$$

where, recall, $S(\boldsymbol{q})$ is the static structure factor. Eq. (7.24) shows that the temporal decay of $S(\boldsymbol{q}, t)$ from $S(\boldsymbol{q})$ is exponential and is characterized by $\boldsymbol{D}(\boldsymbol{q})$. Eq. (7.24) is identical for equilibrium suspensions [33, 70, 71]. Note that the zero wave-number limit of $\boldsymbol{D}(\boldsymbol{q})$ is the suspension collective diffusivity, describing how particles migrate in a weak concentration gradient, i.e., $\boldsymbol{d}_c = \lim_{|\boldsymbol{q}| \to 0} \boldsymbol{D}(\boldsymbol{q})$. At the wave number q_m corresponding to the peak of the static structure factor $S(\boldsymbol{q})$, the wave number dependent diffusivity is believed to describe the cage dynamics in the suspension [34, 72]. At length scale smaller than a single particle, i.e., $|q| \to \infty$, $\boldsymbol{D}$ approaches the long-time self-diffusivity.

In this work, we are interested in the collective diffusion behaviors. However, reaching the limit of $|\boldsymbol{q}| \to 0$ is challenging as the accessible wave numbers are integer multiples of $q_{\min} = 2\pi/L$. Alternatively, we focus on the diffusivities along the 2- and 3-direction with the minimum accessible wave number, $D_{kk}(q_{\min})$ with $k = 2, 3$. We define

$$f_{kk}(q, t) = -q^{-2} \ln[S_{kk}(q, t)/S_{kk}(q)], \tag{7.25}$$

and

$$D_{kk}(q) = \lim_{t \to \infty} \frac{\mathrm{d}}{\mathrm{d}t} f_{kk}(q, t). \tag{7.26}$$

The diffusivities $D_{kk}(q_{\min})$ approximate the suspension collective behavior on the scale of the simulation box.

Fig. 7.6b shows $D_{22}(q_{\min})/d_0$ (open symbols) and $D_{33}(q_{\min})/d_0$ (filled symbols) as functions of Pe_σ at $\bar{\Pi} = 50$. The results are more scattered compared to the long-time self-diffusivities in Fig. 7.6a due to the difficulties associated with the measurement. Compared to d^s_∞ in Fig. 7.6a, $D(q_{\min})$ is in general slightly higher at the same Pe_σ, but shares the same pattern with respect to changes in Pe_σ: grows with Pe_σ for amorphous flowing suspensions, and decreases with Pe_σ in the string phase, suggesting that the diffusive behaviors of dense suspensions are consistent at different length scales. Note that, for equilibrium suspensions at low to moderate concentration, d^s_∞ decreases while d_c grows with increasing ϕ.

The inset of Fig. 7.6b presents the time evolution of the function f_{kk} with $k = 2$ (dashed lines) and 3 (solid lines) in Eq. (7.25). As expected, at a time scale comparable to a^2/d_0, f_{kk} becomes linear in time for flowing suspensions in both the 2- and 3-directions. In the string phase, f_{kk} is qualitatively different. In particular, the difference between f_{22} and f_{33} are more significant, suggesting that the anisotropic string structures influence the collective diffusion differently in different directions. Moreover, for arrested suspensions, f_{kk} is not diffusive within the observation time frame. Indeed, the temporal evolution of f_{kk} shares strong similarity with $\left\langle \Delta x_k^2 \right\rangle$ in Fig. 7.6a.

A third characterization of the suspension dynamics, usually from dynamic light scattering experiments, is the self-intermediate scattering function $F_s(\boldsymbol{q}, t)$, averaged over all the available time. The function F_s is defined as

$$F_s(\boldsymbol{q}, t) = \frac{1}{N} \sum_i \left\langle \exp\{i\boldsymbol{q} \cdot [\boldsymbol{x}_i(t) - \boldsymbol{x}_i(0)]\} \right\rangle . \tag{7.27}$$

For dilute suspensions, $F_s \sim \exp(-d_0 q^2 t)$ due to the particle Brownian motion [1]. The decay of F_s characterizes how fast a particle in the suspension "forgets" where it has been, and, as is customary, characterized by the α-relaxation time τ_α when $F_s = e^{-1}$ [4]. Fig. 7.6c presents the α-relaxation times $\tau_{\alpha,kk}$ with $k = 2$ (open symbols) and 3 (filled symbols) as functions of Pe_σ at $\bar{\Pi} = 50$. Here, τ_α is computed at $qa = 3.5$, corresponding to a wave number near the peak of the static structure factor. This relaxation time characterizes the suspension "cage-breaking" dynamics.

The relaxation time $\tau_{\alpha,22}$ and $\tau_{\alpha,33}$ are similar to each other, with only quantitative differences in the string phase. As soon as the suspension becomes flowing, τ_α be-

comes finite, and quickly reduces with increasing stress for amorphous suspensions. When the suspension enters the string phase at $\mathrm{Pe}_\sigma > 500$, τ_α in both directions grows significantly, suggesting that the structural formation qualitatively affects the cage relaxation process. In fact, the changes in τ_α with respect to Pe_σ are consistent with those of d^s_∞, and Fig. 7.6a and 7.6c resemble top-down mirror images of each other.

The inset of Fig. 7.6c shows the self-intermediate scattering function F_s for extracting τ_α at selected Pe_σ. For an arrested suspension at $\mathrm{Pe}_\sigma = 115$, F_s does not decay significantly over an extended period of time. For flowing suspensions, on the other hand, the decay becomes faster with increasing Pe_σ. Note that with the formation of the string phase, the decay of F_s becomes qualitatively different.

Further information on the suspension dynamics can be extracted from the dynamic susceptibility, χ_4 [37],

$$\chi_4(\boldsymbol{q},t) = N\left[\left\langle\left(\frac{1}{N}\sum_i \exp\{i\boldsymbol{q}\cdot[\boldsymbol{x}_i(t)-\boldsymbol{x}_i(0)]\}\right)^2\right\rangle - \left\langle\frac{1}{N}\sum_i \exp\{i\boldsymbol{q}\cdot[\boldsymbol{x}_i(t)-\boldsymbol{x}_i(0)]\}\right\rangle^2\right] \tag{7.28}$$

which is closely related to the 4-point correlations in the suspension. The peak height of χ_4, $\max(\chi_4)$, is an important indication of dynamic heterogeneities in dense systems [4]. For glassy systems without imposed shear [22, 37, 73], $\max(\chi_4)$ is found to grow significantly near the glass transition. For sheared athermal systems interacting with soft potentials [39, 40], a real-space counterpart of $\max(\chi_4)$ is also found to grow near the jamming point. Therefore, $\max(\chi_4)$ may effectively characterize the flow-arrest transitions of dense systems regardless of underlying driving mechanisms. Fig. 7.6d shows $\max(\chi_4)$ in the 2- (open symbols) and the 3-directions (filled symbols) as functions of Pe_σ with $\bar{\Pi} = 50$. The inset of Fig. 7.6d shows the temporal evolution of χ_4 in both directions.

The peak of the dynamic susceptibility, $\max(\chi_4)$ decreases significantly with increasing Pe_σ in both the 2- and the 3-direction. The reduction in $\max(\chi_4)$ suggests the heterogeneities and fluctuations in the suspension become less significant. The flow-arrest transitions in our systems are similar to the glass and the jamming transitions in other systems. However, as the suspension enters the string phase, $\max(\chi_4)$ increases drastically again and then decreases. This shows that near the

amorphous-string transition, another dynamic heterogeneity emerges in the suspension dynamics.

Moreover, the temporal evolution of χ_4, shown in Fig. 7.6d inset, suggests that for arrested suspensions, e.g., at $\mathrm{Pe}_\sigma = 115$, χ_4 does not grow within the simulation time frame as the particles are essentially locked in place and are unable to organize large-scale fluctuations. For suspensions at $\mathrm{Pe}_\sigma = 145$, χ_4 exhibits a prominent peak at time $\sim a^2/d_0$. However, with increasing Pe_σ, the corresponding χ_4 reaches the peak at an earlier time, and the height of the peak is much lower, because as the suspension begins to flow, the particles do not need large-scale coordination to achieve diffusive motion. In the string phase at $\mathrm{Pe}_\sigma = 1000$ and 1500, the peak of χ_4 increases again, and the qualitative features of χ_4 are different, with more prominent difference between the 2- and the 3-directions comparing to amorphous phase results.

Fig. 7.6 shows the different facets of suspension dynamics in constant stress and pressure rheology. The various characterizations are consistent for flowing suspensions, and the differences between the 2- and 3-directions are negligible. However, structural development qualitatively changes the diffusive dynamics. To study the influence of pressure on the suspension rheology, we focus only on the amorphous suspensions, and from Fig. 7.6, we also focus only on the dynamics in the vorticity direction.

7.4 Dynamics near flow-arrest transitions

Here we investigate the suspension dynamics near the flow-arrest transitions. We focus on a few $(\bar{\Pi}, \mathrm{Pe}_\sigma)$ pairs with $\bar{\Pi} = 50$ and 5 by performing at least 50 independent simulations with distinct initial conditions for analysis.

Temporal heterogeneity

Fig. 7.7 shows the accumulated strain γ from different simulations at $(\bar{\Pi}, \mathrm{Pe}_\sigma) = (50, 145)$, illustrating the unstable suspension behaviors near flow-arrest transitions. The qualitative features of γ in each simulation is similar to those in the inset of Fig. 7.2a: the suspension switches between the flowing and the arrested states, leading to the intermittent growth and stagnation of γ with respect to time. In some cases, the suspension is completely stuck and is unable to flow. These unstable behaviors lead to distinct γ trajectories in each simulation. The average γ trajectory over 50 simulations is shown as a dashed line in Fig. 7.7. In an average sense, $\gamma \propto t$, and only reaches $\gamma \approx 12$ at $t\sigma/\eta_0 = 5000$, suggesting a highly viscous suspension.

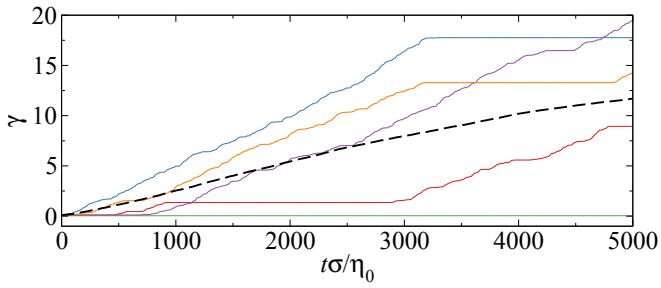

Figure 7.7: (Color online) The time evolution of the accumulated strain γ with $(\bar{\Pi}, \mathrm{Pe}_\sigma) = (50, 145)$. Different solid lines represent results from different runs. The dashed lines are averaged from 50 independent runs.

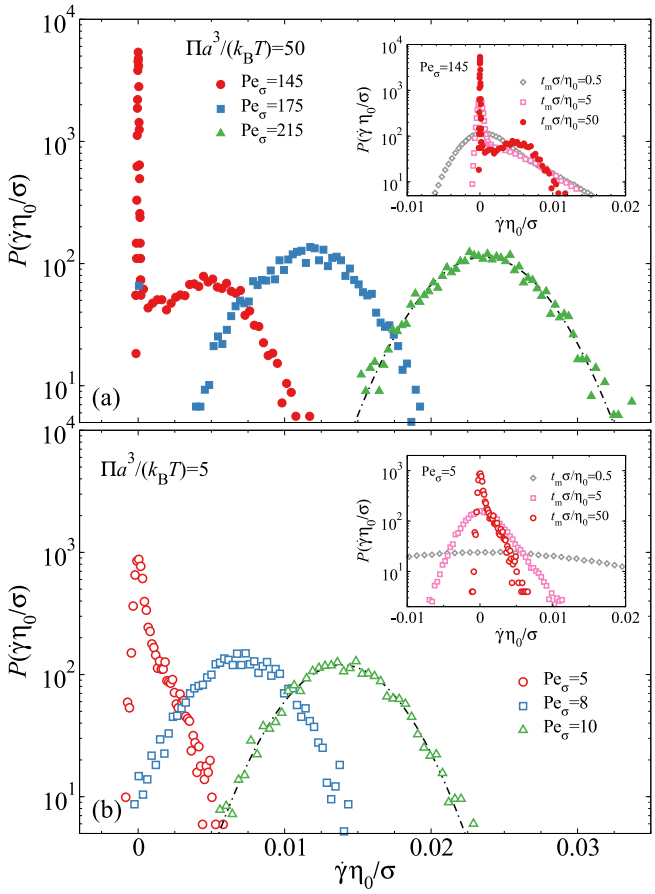

Figure 7.8: (Color online) The probability distribution of the strain rate $\dot{\gamma}\eta_0/\sigma$ at various Pe_σ with the averaging time $t_m\sigma/\eta_0 = 50$. The imposed pressures are $\bar{\Pi} = 50$ (a) and $\bar{\Pi} = 5$ (b). The inset shows the strain rate distribution with different averaging time t_m at the annotated Pe_σ.

Assuming that the unstable dynamics in Fig. 7.7 arises from a stationary process,

the temporal heterogeneity can be analyzed by populating the strain rate probability distribution, $P(\dot{\gamma})$, at different imposed pressures and stresses. However, directly populating the instantaneous strain rate $\dot{\gamma}$ leads to an uninteresting broad, Gaussian-like distribution. Although the instantaneous $\dot{\gamma}$ is strongly affected by noise, the smooth accumulated strain γ suggests that the noise in $\dot{\gamma}$ strongly cancels each other in consecutive times. Therefore, we average the strain rate over an intermediate time t_m, and populate the probability distribution of the average strain rate $\dot{\gamma}$ from independent segments of t_m. For example, the inset of Fig. 7.8a shows the probability $P(\dot{\gamma})$ averaged over time intervals $t_m\sigma/\eta_0 = 0.5$, 5, and 50 at $(\bar{\Pi}, \mathrm{Pe}_\sigma) = (50, 145)$. With increasing t_m, $P(\dot{\gamma})$ becomes narrower and develops split peaks. At $t_m\sigma/\eta_0 = 0.5$, the distribution $P(\dot{\gamma})$ is asymmetric, with a positive peak close to $\dot{\gamma} = 0$, and a tail skewed towards positive $\dot{\gamma}$, leading to an overall positive average $\dot{\gamma}$. Increasing $t_m\sigma/\eta_0$ to 5, the peak near $\dot{\gamma} = 0$ becomes significantly narrower, and a skewed tail remains for $\dot{\gamma} > 0$. When $t_m\sigma/\eta_0 = 50$, $P(\dot{\gamma})$ shows two contributions: a narrow distribution around $\dot{\gamma} = 0$, and a wide distribution with a different peak at $\dot{\gamma} > 0$. At this t_m, the noise is suppressed to reveal the origin of the asymmetry in $P(\dot{\gamma})$ at smaller t_m. The strain rate distribution shows that, near the flow-arrest transition, the suspensions switches between an arrested state with a narrow strain rate distribution centered at $\dot{\gamma} = 0$ and a flowing state with a wider $\dot{\gamma}$ distribution centered at $\dot{\gamma} > 0$. Switching between the flowing and the arrest states leads to the γ instability in Fig. 7.7. Approximating both contributing distributions as normal distribution $\mathcal{N}(\mu, \sigma)$ with mean μ and variance σ^2, we have

$$P(\dot{\gamma}) \approx w_A \mathcal{N}(0, \sigma_A) + (1 - w_A)\mathcal{N}(\dot{\gamma}_F, \sigma_F), \tag{7.29}$$

with $\sigma_F \gg \sigma_A$, $\dot{\gamma}_F > 0$, and w_A the proportion of the arrested states. In Fig. 7.8, w_A can be estimated by integrating over the peak centered at $\dot{\gamma} = 0$. Eq. (7.29) suggests that the suspension dynamics might be modeled as a reaction system with distinct flowing and arrested states via non-equilibrium statistical physics [74]. However, this is beyond the scope of the current work.

The main figure of Fig. 7.8a also presents $P(\dot{\gamma})$ at $\mathrm{Pe}_\sigma = 175$ and 215. The contributions from the arrested state quickly diminishes, i.e., $w_A \to 0$ as the imposed stress exceeds the yield stress $\sigma \gg \sigma_m$. A small arrest peak in $P(\dot{\gamma})$ remains visible at $\mathrm{Pe}_\sigma = 175$, but it completely vanishes at $\mathrm{Pe}_\sigma = 215$. Indeed the strain rate distribution at $\mathrm{Pe}_\sigma = 215$ can be fitted to a normal distribution, which is shown in dashed-dotted line in Fig. 7.8. Away from the flow-arrest transition, the strain rate distribution in the flowing state appears to follow a random Gaussian process.

To highlight the influences of $\bar{\Pi}$, Fig. 7.8b presents $P(\dot{\gamma})$ at $\bar{\Pi} = 5$ with the same t_m. Although the qualitative features are similar to Fig. 7.8a, reducing $\bar{\Pi}$ shows an increase in the fluctuations. Near the flow-arrest transition, i.e., at $\mathrm{Pe}_\sigma = 5$, $P(\dot{\gamma})$ has two contributions, and can be approximated via Eq. (7.29). Compared to the $P(\dot{\gamma})$ at $(\bar{\Pi}, \mathrm{Pe}_\sigma) = (50, 145)$, the most distinguishing feature here is that σ_A associated with the arrested state is larger, and σ_F associated with the flowing state is smaller. Consequently, the instability between the flowing and the arrested states in $\gamma(t)$ is less evident compared to $\bar{\Pi} = 50$. At higher Pe_σ, $P(\dot{\gamma})$ becomes broader due to the stronger thermal fluctuations. Furthermore, the inset of Fig. 7.8b presents the effect of t_m on $P(\dot{\gamma})$ near the flow-arrest transition. Increasing t_m show similar effects on $P(\dot{\gamma})$ as the case of $\bar{\Pi} = 50$, but the lower confining pressure leads to stronger thermal fluctuations at small t_m.

Fig. 7.8 shows that the instability in γ near the flow-arrest transition arises from the suspension switching between a flowing state and an arrested state. These behaviors are present at both low and high confining pressures, but are more pronounced at high $\bar{\Pi}$ due to the weaker thermal fluctuations. The strain rate distribution is sensitive to the averaging time t_m, and can be approximated using Eq. (7.29) with sufficiently large t_m. The weight w_A in Eq. (7.29) rapidly vanishes as the suspension leaves the flow-arrest transition. However, understanding how Eq. (7.29) is affected by the imposed stresses and pressures from a first principle perspective remains a challenge.

Fig. 7.8 also reveals that each $(\bar{\Pi}, \mathrm{Pe}_\sigma)$ pair covers a strain rate range which reduces with increasing averaging time t_m. Therefore, the suspension behaviors over the a range of $\dot{\gamma}$ can be analyzed with the same imposed stress and pressure. This is different from the start-up or the cessation studies, where the suspension responses at different $\dot{\gamma}$ is found through a sudden change in the external forcing. The results from the two approaches are equivalent in the linear response regime, but their relation for non-equilibrium systems is unclear.

We analyze the suspension behaviors at different $\dot{\gamma}$ for each $(\bar{\Pi}, \mathrm{Pe}_\sigma)$ pair with $t_m = 50\eta_0/\sigma$, which is long enough to suppress the thermal noises, but is also short enough for adequately sampling the suspension responses at each $\dot{\gamma}$. The suspension properties are computed from different simulation segments with same average $\dot{\gamma}$. Fig. 7.9a and 7.9b show the volume fraction ϕ and long-time self-diffusivity in the vorticity direction d^s_∞, respectively, as functions of the strain rate $\dot{\gamma}\eta_0/\sigma$ for $\mathrm{Pe}_\sigma = 145$, 175, and 215 at $\bar{\Pi} = 50$ and $\mathrm{Pe}_\sigma = 5$, 8, and 10 at $\bar{\Pi} = 5$. The diffusivity

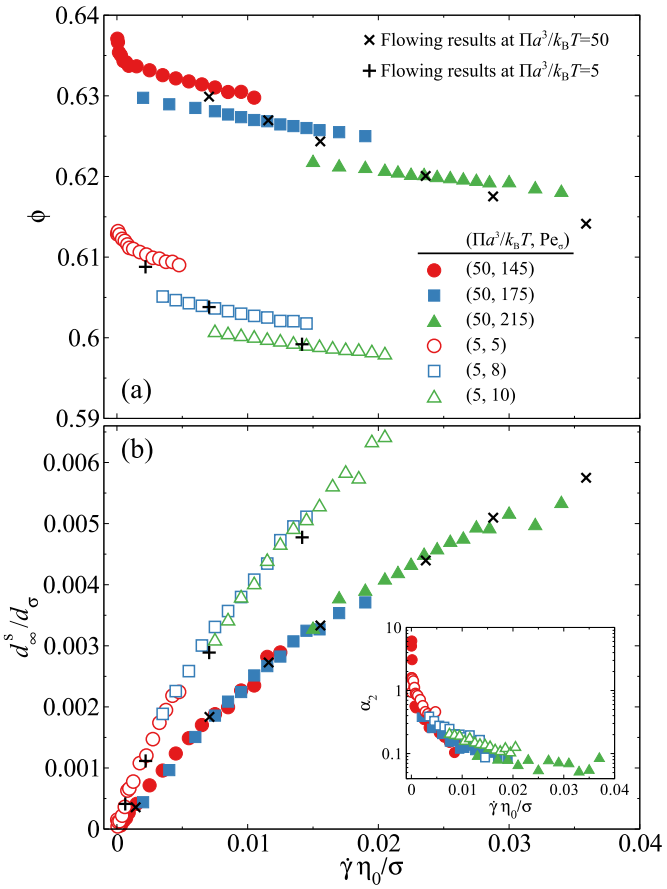

Figure 7.9: (Color online) The volume fraction, ϕ (a), and the stress scaled long-time self-diffusivity in the vorticity direction, $d^s_\infty \eta_0/(a^2\sigma)$ (b), as functions of the time-averaged strain rate $\dot{\gamma}\eta_0/\sigma$ in simulations at Pe_σ = 145, 175, and 215 for $\bar{\Pi}$ = 50 and at Pe_σ = 5, 8, 10 for $\bar{\Pi}$ = 5. The averaging time $t_m\sigma/\eta_0$ = 50. The crosses and pluses symbols are results averaged from the entire simulations at these pressures. The inset of (b) presents the corresponding non-Gaussian parameter α_2 as a function of $\dot{\gamma}\eta_0/\sigma$ measured at $t_m\sigma/\eta_0$ = 50.

in Fig. 7.9b is scaled with the stress diffusion scale,

$$d_\sigma = a^2\sigma/\eta_0, \tag{7.30}$$

to highlight the influence of the imposed stress. In Fig. 7.9, the scaled strain rate is the inverse shear viscosity, $\dot{\gamma}\eta_0/\sigma = \eta_0/\eta_s$. Also presented in Fig. 7.9 are ϕ and d^s_∞ averaged over the multiple simulations from Fig. 7.13b and Fig. 7.16a, shown as crosses for $\bar{\Pi}$ = 50 and pluses for $\bar{\Pi}$ = 5. Near the flow-arrest transitions, the ϕ and d^s_∞ curves can assess the suspension properties at much lower $\dot{\gamma}\eta_0/\sigma$ comparing to direct simulation-wide averages. Therefore, the analysis here is suitable for studying suspension dynamics near the flow-arrest transitions.

In Fig. 7.9a, each $(\bar{\Pi}, \mathrm{Pe}_\sigma)$ pair corresponds to a unique $\phi(\dot{\gamma})$ curve that does not overlap each other. In general, increasing $\dot{\gamma}$ leads to a ϕ decrease due to suspension dilation. Close to the flow arrest transition $\dot{\gamma} = 0$, the volume fraction ϕ becomes sensitive to $\dot{\gamma}$, and increases rapidly with diminishing $\dot{\gamma}$. This is particularly obvious at $(\bar{\Pi}, \mathrm{Pe}_\sigma) = (50, 145)$. At lower imposed pressure, the arrest volume fraction is reduced. The simulation-wide averages are always on the $\phi(\dot{\gamma})$ curves, except near the flow-arrest transitions due to the arrested states. On the other hand, in Fig. 7.9b, the dimensionless diffusivity d^s_∞/d_σ at different Pe_σ collapses to a master curve at the same $\bar{\Pi}$. The results also agree with the simulation-wide averages shown in the crosses and pluses at $\bar{\Pi} = 50$ and 5, respectively, justifying the adopted time frame $t_m = 50\eta_0/\sigma$.

We further characterize the suspension dynamics by computing the non-Gaussian parameter $\alpha_2(t)$ [75, 76] in the vorticity direction,

$$\alpha_2(t) = \frac{\left\langle \Delta x_3(t)^4 \right\rangle}{3\left\langle \Delta x_3(t)^2 \right\rangle^2} - 1, \tag{7.31}$$

which is presented in the inset of Fig. 7.9b at $t = t_m$. The non-Gaussian parameter α_2 becomes non-zero when the particle movement Δx_3 deviates from being fully diffusive, and is the real space equivalence of the dynamic susceptibility $\chi_4(t)$. A high α_2 suggests strong collective particle motions [75].

The inset of Fig. 7.9b shows that α_2 decreases from a large value at $\dot{\gamma}\eta_0/\sigma \approx 0$ with increasing $\dot{\gamma}$. Near the flow-arrest transition, the low d^s_∞ and the high α_2 suggests that the particles are locked by their neighbors and can only move around with collective motion. When $\dot{\gamma}\eta_0/\sigma \gg 0$, $\alpha_2 \ll 1$ and d^s_∞ is well defined, suggesting that the particles can diffuse in the 3-direction. Moreover, the non-Gaussian parameter α_2 at different $(\bar{\Pi}, \mathrm{Pe}_\sigma)$ pairs almost collapses, suggesting that the higher order particle dynamics are similar despite the different d^s_∞, and are principally determined by the strain rate.

Fig. 7.9 shows that, at a fixed imposed pressure Π, the volume fraction is a function of both the strain rate and the shear stress, $\phi = \phi(\dot{\gamma}, \sigma; \Pi)$, but the dimensionless diffusivity $\varrho = d^s_\infty/d_\sigma$ is only a function of the strain rate, $\varrho = \varrho(\dot{\gamma}; \Pi)$. Therefore, in constant stress and pressure rheology, the dimensionless diffusivity q does not have explicit dependence on the shear stress σ and the volume fraction ϕ, and can only be affected by changing $\dot{\gamma}$ and Π. With constant imposed stress, the average volume fraction $\langle\phi\rangle$ and the average diffusivity $\langle d^s_\infty\rangle$ are computed using the strain rate probability $P(\dot{\gamma})$ as $\langle\phi\rangle = \int \phi(\dot{\gamma}, \sigma; \Pi) P(\dot{\gamma}) \mathrm{d}\dot{\gamma}$ and

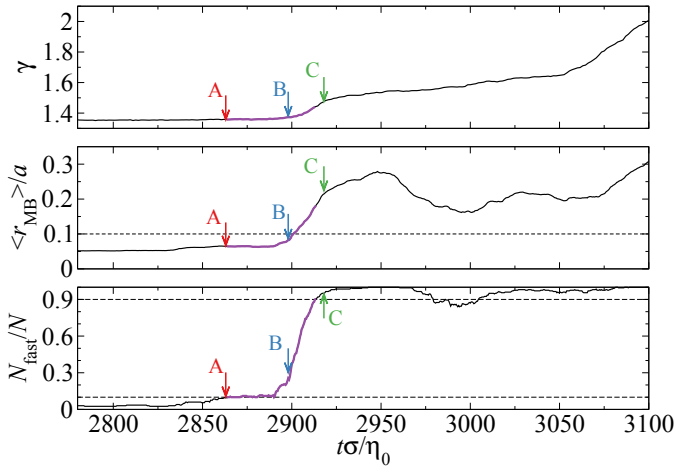

Figure 7.10: (Color online) Typical time evolution of a suspension at $\mathrm{Pe}_\sigma = 145$ and $\bar{\Pi} = 50$ near an arrest-event transition: (top) the accumulated strain γ; (center) the average radius of the minimum enclosing circle of the particle trajectory $\langle r_{\mathrm{MB}} \rangle$; (bottom) the fraction of the fast particles N_{fast}/N. In computing r_{MB}, the trajectory of the past $50\eta_0/\sigma$ time units in the velocity gradient-vorticity plane are considered. The transition from the flowing to the arrested states are highlighted, with the arrows pointing out three time instances A, B, and C. The horizontal dashed lines highlight the cutoff radius r_c in the middle panel and the lower and upper limiting fast particle fractions.

$\langle d_\infty^s \rangle = d_\sigma \int \varrho(\dot{\gamma}; \Pi) P(\dot{\gamma}) \mathrm{d}\dot{\gamma}$. For constant strain rate rheology with the corresponding stress distribution $\hat{P}(\sigma)$, the average volume fraction is similar to the case of constant stress, $\langle \phi \rangle = \int \phi(\dot{\gamma}, \sigma; \Pi) \hat{P}(\sigma) \mathrm{d}\sigma$. However, the average diffusivity becomes $\langle d_\infty^s \rangle = a^2 \varrho(\dot{\gamma}; \Pi) \langle \sigma \rangle / \eta_0$, allowing a direct connection between the suspension mechanics $\langle \sigma \rangle$ and the particle diffusion $\langle d_\infty^s \rangle$.

Spatial heterogeneity

The flow-arrest instability in the accumulated strain $\gamma(t)$ in Fig. 7.7 provides a unique opportunity to study the particle-level details of the *spontaneous* arrest-flow events, which, as we have mentioned, are distinct from the transient response in start-up or cessation studies. Here, the imposed stresses and pressures are fixed and the events entirely arise from the fluctuations of the system.

An arrest-flow event is defined as the shortest continuous time where the suspension changes from an arrested state to a flowing state. These states are based on the fraction of fast particles in the suspension, N_{fast}/N, i.e., in an arrested state $N_{\mathrm{fast}}/N \leq 10\%$ and in a flowing state $N_{\mathrm{fast}}/N \geq 90\%$. Fig. 7.10 illustrates a typical event from

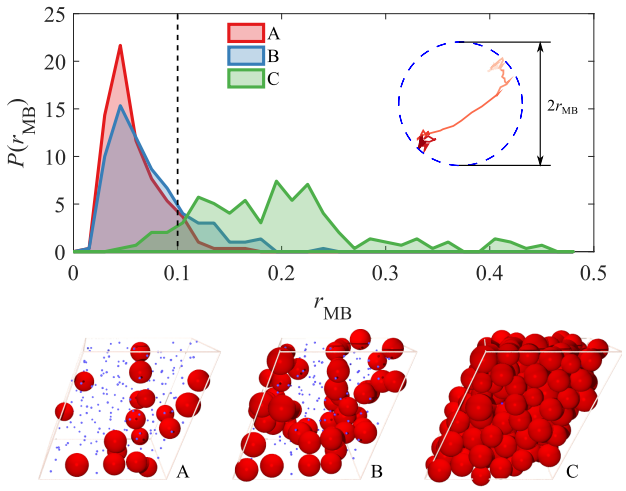

Figure 7.11: (Color online) (Top panel) The probability distribution of the radius of the minimum enclosing circle r_{MB} at time instances A, B, and C highlighted in Fig. 7.10. The cutoff radius r_c is shown in the vertical line. Also shown are the definition of r_{MB} and a typical particle trajectory, with more recent positions in darker color. (Bottom panel) The suspension snapshots at instances A, B, and C. The "fast" particles are shown in red in their full size, and the remainder are shown as blue dots.

point A to point C at $(\bar{\Pi}, \mathrm{Pe}_\sigma) = (50, 145)$, with the bottom panel showing the time evolution of N_{fast}/N. The exact choice of the cutoff fractions (10% and 90%) does not affect the spatial features of the event, but must ensure sufficient samples for analysis.

To determine N_{fast}, we analyze the particle trajectory projected to the 23-plane (velocity gradient-vorticity plane) over the past t_m time and compute the radius of the minimum enclosing circle r_{MB}, such that the distance between any two points in the trajectory does not exceed $2r_{MB}$. We consider a particle *fast* if its corresponding r_{MB} is larger than a cutoff radius r_c. Here, we choose the past time duration $t_m = 50\eta_0/\sigma$, and $r_c = 0.1a$. A typical particle trajectory projected into the 23-plane is shown in the top panel of Fig. 7.11. The current location at time t is red, and the color on the trajectory gradually fades to white at time $t - t_m$. The computed minimum enclosing circle [77] is shown in the dashed circle. Note also that the exact choice of r_c does not affect the results significantly.

The middle panel of Fig. 7.10 presents the time evolution of $\langle r_{MB} \rangle$ averaged over all particles as a function of time during the arrest-flow event. The dashed line represents the cutoff radius r_c. As the suspension changes from the arrested state

to the flowing state, $\langle r_{\mathrm{MB}} \rangle$ increase from below r_c to above. In addition, the top panel of Fig. 7.10 shows the accumulated strain γ as a function of time, which grows appreciably as the suspension becomes flowing. Changes in γ and $\langle r_{\mathrm{MB}} \rangle$ during the arrest-flow event are consistent with the N_{fast}/N evolution. However, defining the arrest-flow event using N_{fast}/N provides a clear duration for the event.

Characterizing the arrest-flow event using *fast* particles is inspired by experiments in colloidal glasses [75], where "mobile" particles move together in clusters as the suspension approaches the glass transition—a direct manifestation of dynamic heterogeneity. The length scale associated with the cluster, ℓ_c, diverges as the system approaches glass transition, because moving one particle out of its neighboring cage requires structural rearrangement in the entire system [15, 78, 79]. Therefore, studying clustering behaviors of mobile particles requires large system sizes to observe the diverging length scale and to eliminate the artifacts from periodic simulation box.

During an arrest-flow event, the fast particles in the suspension grow from a few to the entire system during a short period of time similarly to glassy dynamics. Taking points A, B, and C in Fig. 7.10 as an example, the top panel of Fig. 7.11 shows the corresponding probability distribution of r_{MB}, $P(r_{\mathrm{MB}})$, with the cutoff radius r_c shown as a vertical dashed line. At the beginning of the event (A), $P(r_{\mathrm{MB}})$ is peaked below r_c, as the majority of the particles are arrested and are confined to their neighboring cages. As the suspension starts flowing (B), the distribution shifts its tail towards higher r_{MB}. At at the end of the event (C), for the flowing suspension $P(r_{\mathrm{MB}})$ becomes much broader, and the majority of $P(r_{\mathrm{MB}})$ lies beyond r_c. The probability distributions at A and C illustrate the distinct flowing and arrested states. The corresponding simulation snapshots are shown in the bottom panel of Fig. 7.11. The fast particles are shown in full sizes and in red, and the other particles are shown as blue dots. Not clear in Fig. 7.11 is how the new fast particles appear.

The spatial organization of fast particles during an arrest-flow event has two possibilities: (1) the fast particles appear randomly in an uncorrelated fashion, suggesting that the flow-arrest transition is structurally independent, and is dominated by the thermal fluctuations; or (2) an arrested particle can only become mobile if its neighbors are also mobile. In this case, the suspension becomes flowing by propagating fast particles, and the arrest-flow event strongly depends on the structure of the fast particle cluster. In this sense, it is similar to the dynamic heterogeneity in a glass: in the thermodynamic limit, the suspension becomes flowing if the correlation length

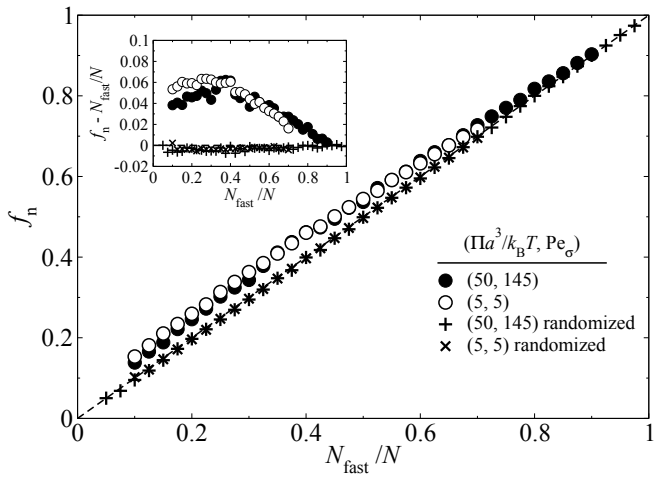

Figure 7.12: The fraction of the neighboring particles of a fast particle that are also fast, f_n, as a function of the fraction of fast particles in the suspension, N_{fast}/N, near the flow-arrest transitions at $(\bar{\Pi}, Pe_\sigma) = (50, 145)$ (filled symbols) and $(5, 5)$ (open symbols). The plus and cross symbols are the results when the fast particles are randomly selected. The inset highlights the difference $f_n - N_{fast}/N$.

of the fast particle cluster $\ell_c \to \infty$.

We analyze the structural details of the arrest-flow events to characterize the emergence of fast particles. The modest system size $N = 200$ makes analyzing the correlation length ℓ_c ineffective. Instead, we compare local behaviors of fast particles to the suspension-wide results. If a fast particle is enclosed by N_n neighboring particles, and N_{nf} of them are also fast moving particles, we define,

$$f_n = N_{nf}/N_n, \tag{7.32}$$

as the fraction of fast neighbors, which inherently depends on the suspension structure. If fast particles appear randomly, we expect $f_n = N_{fast}/N$. Otherwise, fast particles prefer to be next to each other if $f_n > N_{fast}/N$, while avoid each other if $f_n < N_{fast}/N$.

Fig. 7.12 presents f_n, defined in Eq. (7.32), as a function of the fraction of fast particles in the suspension, N_{fast}/N, which also gauges the progression of the arrest-flow events since the time duration of these events varies. The results are averaged over all available events at $(\bar{\Pi}, Pe_\sigma) = (50, 145)$ and $(5, 5)$. The neighboring particles are identified using radical tessellation [80], and the fast particles are found using their trajectories on the 23-plane. At $(\bar{\Pi}, Pe_\sigma) = (5, 5)$, the arrest-flow event is defined as the transition between $N_{fast}/N = 0.1$ and 0.7 due to stronger thermal

fluctuations. Fig. 7.12 also shows the "randomized" results by randomly assigning fast particles within the same sequences of particle configurations. As expected, the randomized results satisfy $f_{\mathrm{n}} = N_{\mathrm{fast}}/N$ as the emergence of the fast particles are independent of the existing fast particle configuration. On the other hand, for actual fast particles, $f_{\mathrm{n}} > N_{\mathrm{fast}}/N$: during an arrest-flow event, fast particles are more likely to appear next to each other. However, the result does not indicate whether a new fast moving particles prefers to appear next to an existing one, as the presence of a fast particle itself is dynamical: it appears and disappears during the arrest-flow event. Furthermore, as the fraction of fast particles becomes large ($N_{\mathrm{fast}}/N > 0.7$), the difference between f_{n} and N_{fast}/N diminishes due to the finite system size.

The emergence of fast particles is similar at different $\bar{\Pi}$, suggesting a universal suspension behavior in arrest-flow events. The inset of Fig. 7.12 quantifies this similarity by showing $f_{\mathrm{n}} - N_{\mathrm{fast}}/N$, which reaches a maximum of ~ 0.06 at $N_{\mathrm{fast}}/N \approx 0.4$. Clearly, when N_{fast}/N is small, the fast particles appear randomly due to mechanical or thermal fluctuations. As N_{fast}/N increases, the fast particles prefer to appear in clusters: the neighbor of a fast particle is more likely to be fast. Although it is difficult to quantify the correlation length from f_{n}, the results do show that cooperative particle rearrangement is necessary for arrest-flow events. The cooperation reaches a maximum at $N_{\mathrm{fast}}/N \approx 0.4$. Beyond that point, $f_{\mathrm{n}} - N_{\mathrm{fast}}/N$ decreases, and the fast moving particles emerge more randomly since a significant portion of the suspension is already fast. However, the cooperative rearrangement is still evident as the differences are higher than the randomized results.

7.5 A granular perspective on Brownian suspension rheology

Adopting a granular perspective, we characterize different aspects of suspension behavior using the viscous number. Focusing on amorphous systems, we exclude from the discussions the results showing string order structures, which exhibit qualitatively different structural and mechanical responses.

Mechanical responses

Fig. 7.13 presents the suspension shear viscosity $\eta_s = \sigma/\dot{\gamma}$, the volume fraction ϕ, and the *macroscopic* friction coefficient $\mu = \sigma/\Pi$ as functions of the viscous number $I_v = \dot{\gamma}\eta_0/\Pi$ for colloidal suspensions under constant imposed shear stress σ and confining pressure Π. In Fig. 7.13, the dimensionless imposed pressure $\bar{\Pi} = \Pi a^3/k_{\mathrm{B}}T = 1$ to 1000, and $I_v < 1$ due to the string order formation at higher I_v.

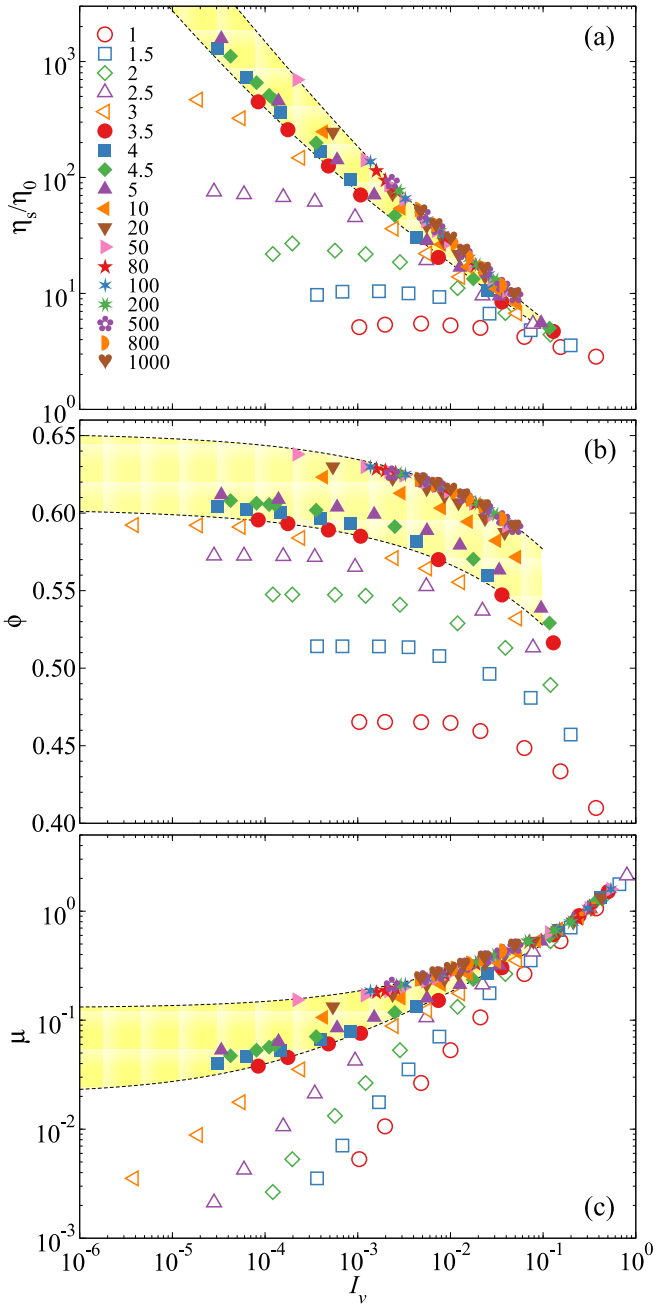

Figure 7.13: (Color online) The suspension shear viscosity η_s/η_0 (a), the volume fraction ϕ (b), and the *macroscopic* friction coefficient μ as functions of the viscous number I_v over a wide range of the imposed pressure $\bar{\Pi}$. The shaded area bounded by dashed lines are from the rheological model in Sec. 7.5, outlining the boundary of glassy suspensions.

The shear viscosity η_s in Fig. 7.13a shows two distinct behaviors in the $I_v \ll 1$ limit: with low imposed pressures $\bar{\Pi} < 3.5$, η_s asymptotes a finite value corresponding to

the at-rest viscosity of the equilibrium suspension with the same osmotic pressure Π. And when $\bar{\Pi} \geq 3.5$, the viscosity diverges $\eta_s \to \infty$ as $I_v \to 0$, suggesting the suspension arrests and becomes solid-like. For convenience, we call the former suspension behaviors liquid-like and the latter glassy, and show liquid-like suspensions as open symbols and glassy suspensions as filled symbols. The shear viscosity η_s decreases with growing I_v, i.e., the suspension shear thins in constant stress and pressure rheology. For both liquid-like and glassy suspensions, η_s at different $\bar{\Pi}$ collapse at high I_v, approaching the solvent viscosity η_0 due to suspension dilation. For glassy suspensions, increasing $\bar{\Pi}$ also show a data collapse at $\bar{\Pi} > 50$, suggesting the emergence of a non-Brownian limiting behavior. The shear viscosity η_s of glassy suspensions at lower $\bar{\Pi}$ are parallel to the collapsed results at small I_v.

Fig. 7.13b presents the volume fraction ϕ as a function of I_v for various $\bar{\Pi}$. At different $\bar{\Pi}$, the behaviors of ϕ are similar and are almost parallel to each other: the suspension dilates with increasing I_v, and approaches an at-rest value in the $I_v \ll 1$ limit. For liquid-like suspensions, this corresponds to the density of an equilibrium suspension with an osmotic pressure of the imposed pressure Π. Unlike the shear viscosity in Fig. 7.13a, ϕ does not collapse at high I_v at different $\bar{\Pi}$, but exhibits distinct limits. The volume fraction does show a high-pressure non-Brownian collapse when $\bar{\Pi} > 20$. The high-pressure limiting behaviors outline a ϕ boundary with respect to I_v corresponding to non-Brownian suspensions. Therefore, for a given viscous number I_v, there is a maximum volume fraction that decreases with increasing I_v. The double limit of $I_v \to 0$ and $\bar{\Pi} \to \infty$ defines the Shear Arrest Point (SAP) [20], where the highest volume fraction in Fig. 7.13b is attained at ϕ_{SAP}.

The *macroscopic* friction coefficient $\mu = \sigma/\Pi$ as a function of the viscous number I_v at different $\bar{\Pi}$ is shown in Fig. 7.13c. Since $\mu = I_v \eta_s/\eta_0$, for liquid-like suspensions with $\bar{\Pi} < 3.5$, the friction coefficient μ grows linearly with I_v in the $I_v \ll 1$ limit, with the slope corresponding to the equilibrium suspension viscosity. For glassy suspensions, as $I_v \to 0$ the friction coefficient approaches a constant μ_m characterizing the ratio of the yield stress σ_m to the imposed pressure. The magnitude of μ_m increases with growing I_v, and approaches the SAP friction coefficient μ_{SAP} as $\bar{\Pi} \to \infty$. When I_v is increased from the $I_v \to 0$ limit, μ emerges from the arrested value μ_m, and the difference $(\mu - \mu_m)$ appears to grow sublinearly with respect to I_v. Further increasing I_v leads to linear μ growth. The friction coefficients μ at different $\bar{\Pi}$ collapses with as the suspension viscosity approaches the solvent viscosity η_0 in Fig. 7.13a.

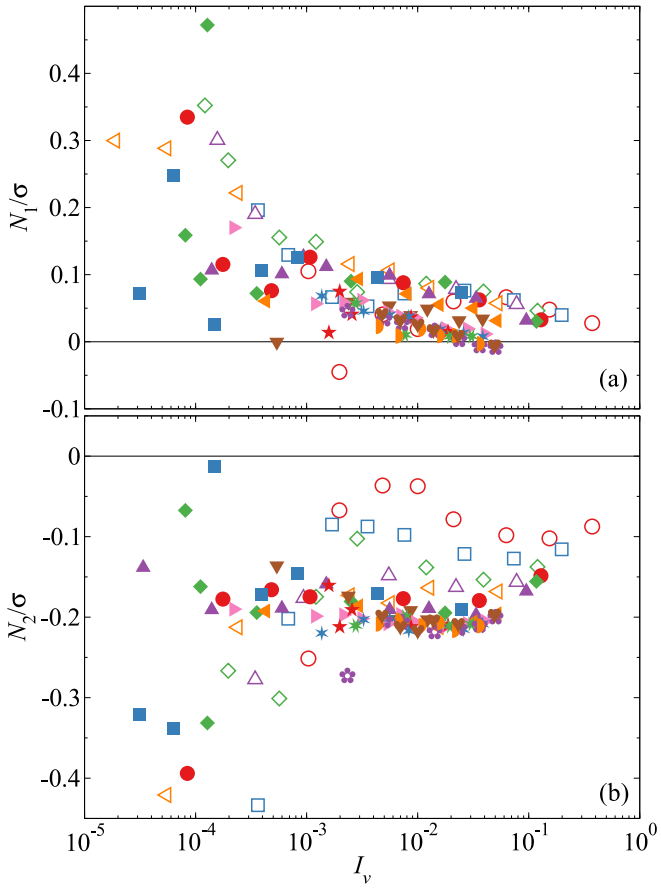

Figure 7.14: (Color online) The stress-scaled normal stress differences N_1/σ (a) and N_2/σ (b) as functions of viscous number I_v for a wide range of imposed pressure $\bar{\Pi}$. The symbols are identical those in Fig. 7.13.

Normal stress differences are another important characterization of the suspensions rheology. The first and the second normal stress differences, N_1 and N_2, defined as,

$$N_1 = \langle \Sigma_{11} \rangle - \langle \Sigma_{22} \rangle \quad \text{and} \quad N_2 = \langle \Sigma_{22} \rangle - \langle \Sigma_{33} \rangle, \tag{7.33}$$

are presented in Fig. 7.14 over a wide range of $\bar{\Pi}$. Consistent with earlier BD studies, N_1 is positive and N_2 is negative. For a simple isotropic material, N_1 and N_2 should emerge from zero as the material is deformed [81, 82]. In simulations, the departure of N_1 or N_2 from zero was not observed due to the difficulties associated with stress differences with significant fluctuations. Scaling the normal stress differences with the imposed stress σ, the results decreases with increasing I_v as the suspension dilates.

In Fig. 7.14a, N_1 appears scattered when $I_v < 0.005$, but the general trend is

deceasing with growing I_v. The positive N_1 is a signature of the dominance of interparticle or Brownian forces in suspensions [51]. If HIs dominant particle interactions, the first normal stress difference $N_1 < 0$ as HIs resist particle pairs to separate. On the other hand, repulsive interparticle forces promotes the pair separation. At higher I_v, N_1 approaches zero as the string-ordered phase formation establishes the fore-aft symmetry in $g(\boldsymbol{r})$ in Fig. 7.3. Moreover, at larger I_v the results at high $\bar{\Pi}$ collapse, showing a universal, non-Brownian N_1 limit.

The second normal stress difference N_2 is negative for all imposed pressures in Fig. 7.14b. For liquid-like suspensions, N_2/σ variation with $I_v < 10^{-3}$ is scattered. The general trend is that the magnitude of N_2/σ decreases. With increasing I_v, the magnitude $|N_2|/\sigma$ reaches a minimum, increases slightly before decreasing again. For glassy suspensions, the results for $I_v > 10^{-3}$ collapses to the non-Brownian limit, where $|N_2|/\sigma$ increases before decreasing again. With increasing $\bar{\Pi}$, $|N_2|/\sigma$ increases, but $|N_1|/\sigma$ decreases, and as $\bar{\Pi} \to \infty$, in general $|N_1| \lesssim |N_2|$. This is consistent with the suspension structural features in Eq. (7.19): for example, in Fig. 7.3, the structural differences near the 1- and 2-axis in g_{12} are more sensitive to Pe_σ relative to those between the 2- and 3-axis in g_{23}. Therefore, the normal stress differences are direct reflection of the suspension structures.

Suspension structures

The suspension structural features, $\max(g_{\mathrm{comp}})$ and $\max(g_{\mathrm{ext}})$, respectively, are presented in Fig. 7.15a and 7.15b for various imposed pressures. According to Eq. (7.19), they are related to the structural contributions to the suspension rheology. Recall that only amorphous suspensions—no string phases—are considered. Beginning with the peak height of g_{comp} in Fig. 7.15a, $\max(g_{\mathrm{comp}})$ is insensitive to I_v due to suspension dilation at low $\bar{\Pi}$, and with increasing I_v, it only increases slightly before decreasing again. At higher $\bar{\Pi}$, $\max(g_{\mathrm{comp}})$ grows but the qualitative features remain unchanged for liquid-like suspensions with $\bar{\Pi} < 3.5$ at low I_v. The peak height $\max(g_{\mathrm{comp}})$ decreases further at higher I_v and collapses with the results at lower $\bar{\Pi}$. For glassy suspensions, $\max(g_{\mathrm{comp}})$ collapses and a high pressure limiting behavior emerges. In this case, $\max(g_{\mathrm{comp}})$ first increases slightly, and then decreases with increasing I_v. Note that $\max(g_{\mathrm{comp}})$ remains finite at finite I_v even as $\bar{\Pi} \to \infty$. In contrast, for monodisperse hard-sphere systems, the contact value of pair distribution function diverges as the system acquires rigidity [83].

The peak values of g_{ext}, presented in Fig. 7.15b, significantly reduce with increasing

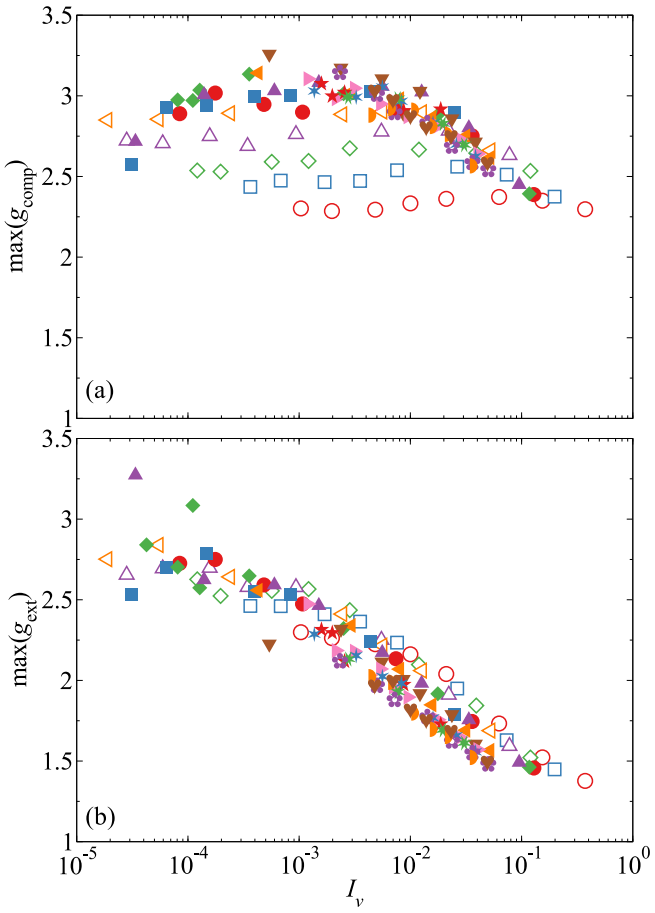

Figure 7.15: (Color online) The peak values of the pair distribution function along the compressional and extensional axes, $\max(g_{\text{comp}})$ (a) and $\max(g_{\text{ext}})$ (b), as functions of the viscous number I_v over a wide range of imposed pressures $\bar{\Pi}$. The symbols are identical to those in Fig. 7.13.

I_v for all $\bar{\Pi}$. In contrast to $\max(g_{\text{comp}})$, $\max(g_{\text{ext}})$ is more sensitive to I_v but less sensitive to $\bar{\Pi}$. This sensitivity grows with increasing I_v, as $\max(g_{\text{ext}})$ reduces faster with higher I_v, and at low I_v, $\max(g_{\text{ext}})$ is almost constant. Furthermore, at the same I_v, increasing $\bar{\Pi}$ in general increases $\max(g_{\text{comp}})$ but reduces $\max(g_{\text{ext}})$. Fig. 7.15 shows the structural features of non-Brownian suspensions in the $\bar{\Pi} \to \infty$ limit: the suspension structural features in the extensional axis, $\max(g_{\text{ext}})$, are more sensitive to I_v, and less sensitive in the compressional axis for $\max(g_{\text{comp}})$.

Diffusive dynamics

Fig. 7.16 presents several suspension diffusive behaviors for various $\bar{\Pi}$, including the long-time self-diffusivity d^s_∞ in Fig. 7.16a, the wave-number dependent diffusivity

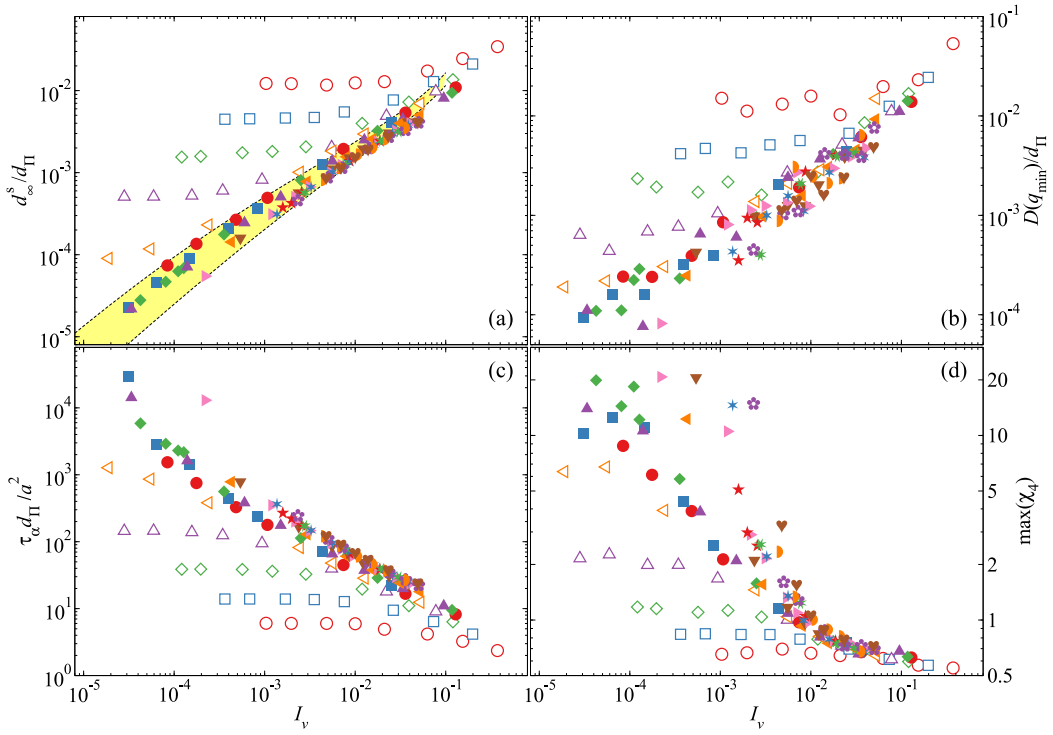

Figure 7.16: (Color online) Different characterizations of suspension dynamics as functions of the viscous number I_v over a wide range of imposed pressures $\bar{\Pi}$. The symbols are identical to those of Fig. 7.13. In (a)–(c) the diffusive quantities are characterized by the pressure diffusion scale $d_\Pi = \Pi a^2/\eta_0$. All the measurements are taken in the vorticity direction. (a): the long-time self-diffusivity d_∞^s/d_Π; (b): the wave-number dependent diffusivity measured at $q_{\min}$, $D(q_{\min})/d_\Pi$; (c): the α-relaxation time $\tau_\alpha d_\Pi/a^2$ from the self-intermediate scattering function at $qa = 3.5$; (d): the peak of the dynamic susceptibility $\max(\chi_4)$. In (a), the shaded area bounded by dashed lines highlights the glassy suspension behaviors from Eq. (7.43).

at the lowest wave number $D(q_{\min})$ in Fig. 7.16b, the α-relaxation time near peak of the static structure factor τ_α in Fig. 7.16c, and peak of the dynamic susceptibility in Fig. 7.16d. Here, we focus on the dynamics in the vorticity direction, since Fig. 7.6 indicated that the dynamics measured from the velocity gradient direction are qualitatively similar. For simplicity, we drop the 33 subscripts in the diffusive quantities. To accommodate the wide range of Brownian and non-Brownian suspension behaviors over a wide range of imposed pressures, we scale the diffusive behaviors with a confining pressure diffusion scale

$$d_\Pi = \dot{\gamma}\eta_0/\Pi. \tag{7.34}$$

Unlike the single-particle diffusivity d_0, the diffusion scale d_Π does not correspond to the diffusivity of an actual diffusion process.

Fig. 7.16a shows the long-time self-diffusivity d^s_∞ as functions of I_v. For liquid-like suspensions, e.g., at $\bar{\Pi} = 1.5$, d^s_∞ grows with I_v from a plateau, which arises from the at-rest suspension diffusion process. Further increasing I_v makes the flow stronger, which eventually overcomes the particle thermal fluctuations, leading to the diffusivity increases with I_v and scales linearly with $\dot{\gamma}$. Upon increasing $\bar{\Pi}$, both the plateau diffusivity and the viscous number where the suspension departs the plateau decrease, e.g., the plateau regimes ends at $I_v \approx 0.005$ for $\bar{\Pi} = 1.5$, and at $I_v \approx 0.0003$ for $\bar{\Pi} = 2.5$. Therefore, the suspension diffusive behaviors are becoming less affected by the at-rest particle dynamics and more affected by the imposed flow. With the emergence of the flow-arrest transition, the diffusivity plateau vanishes, and d^s_∞ only grows with I_v. Further increasing $\bar{\Pi}$ reduces the diffusivity, and the results in the $\bar{\Pi} \gg 1$ limit collapse to a non-Brownian limiting behavior. The high-pressure d^s_∞ are almost parallel to each other, suggesting that the particle diffusion is driven by the external flow, and the at-rest particle dynamics contribute little. The results at high I_v for different $\bar{\Pi}$ also collapse to the dilute diffusion behaviors. Also presented in Fig. 7.16a as yellow shade is the glassy diffusive behaviors predicted by Eq. (7.43), with the dashed lines representing the glass and the jamming limiting behaviors. The predicted diffusion boundary agrees well with the simulation results.

Fig. 7.16b presents the collective suspension diffusive behaviors in the vorticity direction, $D(q_{\min})$, for various $\bar{\Pi}$. Although at different ϕ the corresponding $q_{\min}$ are different, such differences do not affect the qualitative results. With respect to I_v, $D(q_{\min})$ is similar to d^s_∞ in Fig. 7.16a despite stronger data scattering as $D(q_{\min})$ is more difficult to measure. For liquid-like suspensions, $D(q_{\min})$ exhibits equilibrium plateaus in the $I_v \to 0$ limit, and increases with I_v afterwards. For glassy suspensions with $\bar{\Pi} \geq 3.5$, the collective diffusivity is lower than the liquid-like suspensions, and in the $\bar{\Pi} \to \infty$ limit, a non-Brownian limit emerges, suggesting the weak influences of thermal fluctuations. The similarity between $D(q_{\min})$ and d^s_∞, which represents the diffusion process at disparate suspension length scales, suggests that the same underlying mechanism drives the suspension diffusive dynamics at various imposed pressures.

Fig. 7.16c shows the α-relaxation time in the vorticity direction, τ_α, defined as the time for the self-intermediate scattering function to decay to $1/e$, for various imposed pressures. The wave number for F_s is taken at $qa = 3.5$, close to the first peak of the static structure factor, and therefore the corresponding τ_α characterizes

the dynamics of nearest neighboring particle cage. Fig. 7.16c is almost an up-down mirror image of d^s_∞ in Fig. 7.16a, showing that a high d^s_∞ corresponds to a low τ_α. Therefore, the suspension dynamics at the length scale of the cages and the single-particle length scale are similar. For liquid-like suspensions, τ_α decreases from a plateau with increasing I_v, and for glassy suspensions, the plateau vanishes. The crossover between the plateau and the decay occurs at different $\bar{\Pi}$. For glassy suspensions, the results at high $\bar{\Pi}$ also collapse in the non-Brownian limit.

Fig. 7.16d characterizes the suspension dynamic heterogeneity via the peak of the dynamic susceptibility $\max(\chi_4)$ in the vorticity direction, with χ_4 defined in Eq. (7.28), also measured at $qa = 3.5$. The dynamic heterogeneity $\max(\chi_4)$ is qualitatively different from other dynamic characterizations in Fig. 7.16a–7.16c. For liquid-like suspensions, $\max(\chi_4)$ decreases from a low I_v plateau with increasing I_v. The value of the low I_v plateau grows with increasing $\bar{\Pi}$, suggesting that the at-rest dynamic heterogeneity grows with $\bar{\Pi}$. With the emergence of the flow-arrest transitions, $\max(\chi_4)$ at low I_v can reach high value, and the low I_v plateau disappears altogether. In this case, the flow of the suspension is dominated by transient large-scale fluctuations in dynamic heterogeneity. For $I_v > 0.01$, $\max(\chi_4)$ at different $\bar{\Pi}$ collapses and quickly decreases below 1, suggesting that the flowing suspensions in this limit lack large-scale fluctuations.

We further explore the quantitative similarity among d^s_∞, $D(q_{\min})$, and τ_α in Fig. 7.17a and 7.17b by showing $D(q_{\min})$ and τ_α, respectively, as functions of the corresponding d^s_∞. Fig. 7.17a presents the diffusivity on the suspension scale, $D(q_{\min})$, as functions of the corresponding diffusivity on the particle scale, d^s_∞, with both along the vorticity direction. The dashed line indicates that $D(q_{\min}) = d^s_\infty$. In general, $D(q_{\min})$ grows linearly with d^s_∞, and $D(q_{\min})$ is slightly higher, suggesting similar diffusion behaviors at different length scales for flowing suspensions. At low d^s_∞, $D(q_{\min})$ does not follow d^s_∞ linearly and is much higher, most likely because the suspension develops large scale fluctuations to help structural rearrangement while at the single-particle level, the particle movement is still limited by the neighboring particle cage. The inset of Fig. 7.17a presents the ratio $D(q_{\min})/d^s_\infty$ as a function of I_v. Although the results scatters due to the difficulties in measuring $D(q)$, they confirm that $D(q_{\min})$ is in generally higher than d^s_∞ for almost all I_v. The diffusivity ratio becomes higher, up to $D(q_{\min})/d^s_\infty \approx 5$, at low I_v, and reduces with growing I_v. The high diffusivity ratio most likely arises from the emergence of flow-arrest transitions. The most significant data scattering is found in glassy suspensions.

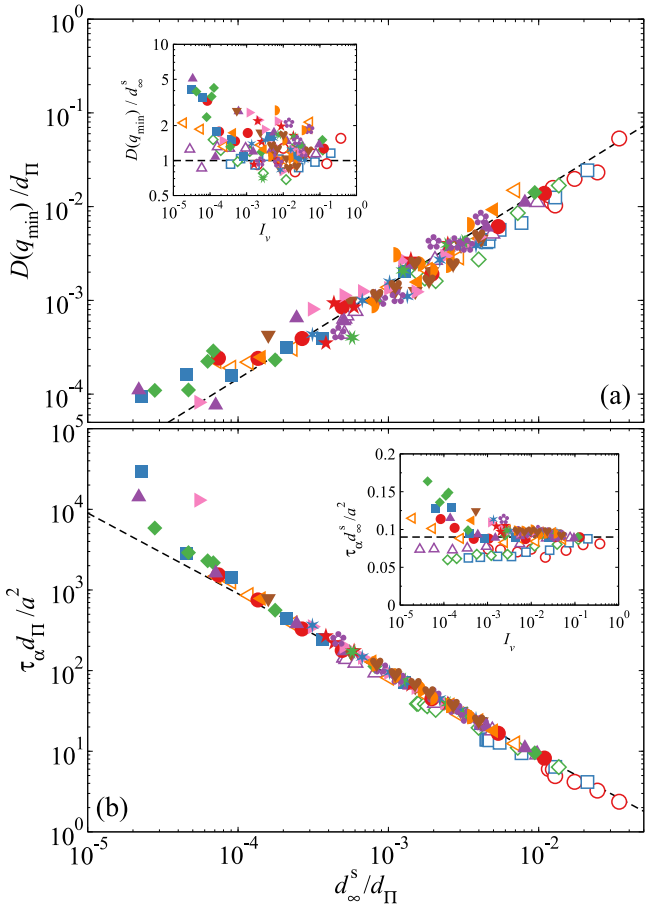

Figure 7.17: (Color online) The wave-number dependent diffusivity measured at $q_{\min}$, $D(q_{\min})$ (a), and the α-relaxation time τ_α (b), as functions of the corresponding long-time self-diffusivity d^s_∞ over a wide range of imposed pressures $\bar{\Pi}$. The symbols are identical to those of Fig. 7.13. The solid line in (a) represents $D(q_{\min}) \propto d^s_\infty$ and in (b) represents $\tau_\alpha^{-1} \propto d^s_\infty$. In the insets, the ratio, $D(q_{\min})/d^s_\infty$ (a), and the product, $\tau_\alpha d^s_\infty$ (b), are presented as functions of I_v. The solid lines in the insets are horizontal. All measurements are taken in the vorticity direction.

Fig. 7.17b presents the connection between τ_α and d^s_∞ in the vorticity direction, with the dashed line outlining $\tau_\alpha^{-1} \propto d^s_\infty$. Fig. 7.17b confirms that τ_α is inversely proportional to d^s_∞, and the results for various $\bar{\Pi}$ collapse onto a single curve. The quality of the collapse is better comparing to Fig. 7.17a, since both d^s_∞ and τ_α describe single-particle behaviors, but $D(q_{\min})$ quantifies the collective suspension behaviors beyond the single-particle level. The relaxation time τ_α deviates from being inversely proportional to d^s_∞ at low d^s_∞, and becomes higher than the dashed line. The inset of Fig. 7.17b shows the product $\tau_\alpha d^s_\infty/a^2$ as functions of I_v over a wide range of $\bar{\Pi}$. At moderate to high I_v, the product is almost a constant insensitive

to I_v. At lower I_v, where the suspensions show an increase in $\max(\chi_4)$, the product becomes more sensitive to I_v. This is especially true for glassy suspensions at higher $\bar{\Pi}$, where the product becomes much higher than the results at high I_v, suggesting longer τ_α, i.e., the diffusion on the cage scale is slower than the single-particle diffusion, consistent with the dynamic heterogeneity description of glass transition [15]. Unlike the glass transition, however, the dynamic heterogeneity arises from both the imposed flow and the particle thermal fluctuations.

Fig. 7.17 quantitatively demonstrates that the diffusion processes at different length scales are consistent for homogeneous flowing suspensions. Unexpected differences arise when the suspensions are near the flow-arrest transitions, because, in this case, the dynamics at various length scales are different.

A model for glassy rheology

The rheology of glassy suspensions at different imposed pressures $\bar{\Pi}$ in Fig. 7.13 shares great similarity in the behaviors near the flow-arrest transitions despite different arrest volume fractions ϕ_m and arrest friction coefficients μ_m. The similarity is especially evident from the almost parallel volume fractions in Fig. 7.13b and the viscosity divergence in Fig. 7.13a. A convenient way to model the suspension behaviors is to express ϕ and μ as,

$$\phi = \phi_m - \delta\phi \quad \text{and} \quad \mu = \mu_m + \delta\mu, \tag{7.35}$$

where the arrest point is (ϕ_m, μ_m). The changes from the arrest point can be expressed as a power law in the viscous number,

$$\delta\phi = K_\phi I_v^{\alpha_\phi} \quad \text{and} \quad \delta\mu = K_\mu I_v^{\alpha_\mu}, \tag{7.36}$$

where the "constants" K_ϕ and α_ϕ characterize $\delta\phi$ and K_μ and α_μ characterize $\delta\mu$: they may, in general, change with the imposed pressure Π. The power law expressions of $\delta\phi$ and $\delta\mu$ in I_v have long been used to characterize the flow of granular materials and non-Brownian suspensions in experiments and in simulations. For example, constant stress and pressure experiments on non-Brownian suspension found that $\alpha_\mu = \alpha_\phi = 0.5$ [26], and experiments in granular matter identified $\alpha_\mu = 1$ [28]. These expressions have been generalized to tensorial forms for continuous modeling the flow behaviors [17]. Moreover, mean-field theories have been developed to predict α_μ and α_ϕ [31].

If the physics of jamming dominates the flow behaviors of the suspensions, Eq. (7.36) should be a reasonable description of the glassy suspension behavior. The weak in-

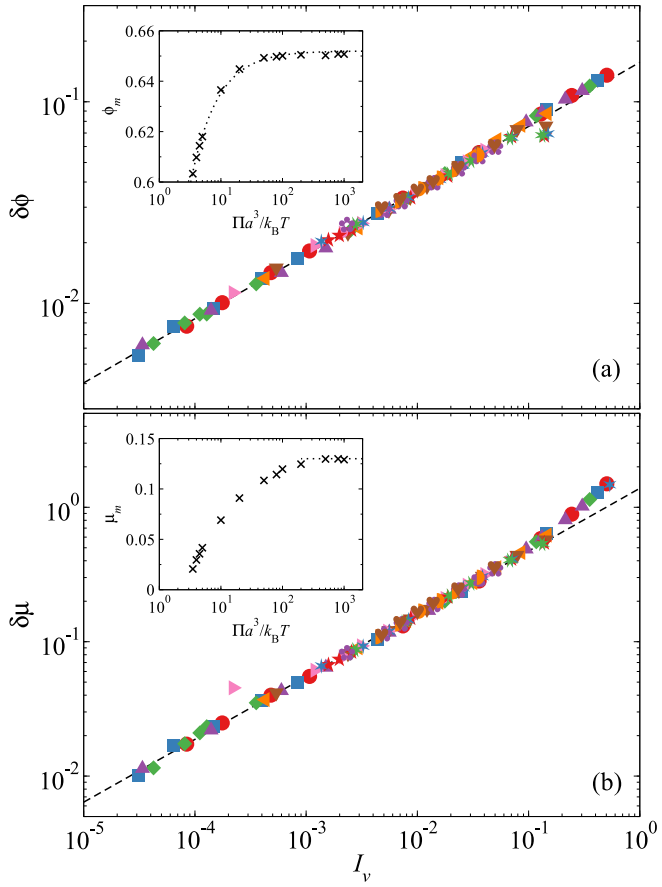

Figure 7.18: (Color online) The incremental volume fraction $\delta\phi = \phi_m - \phi$ (a) and the incremental friction coefficient $\delta\mu = \mu - \mu_m$ (b) as functions of the viscous number I_v for glassy suspensions with $\bar{\Pi} \geq 3.5$. The dashed lines in the main figures highlight the power law relation of Eq. (7.36). The insets show the limiting volume fraction ϕ_m (a) and the limiting friction coefficient μ_m (b) as functions of the imposed pressure $\bar{\Pi}$. The dashed line in the inset of (a) shows Eq. (7.37), and the dashed line in the inset of (b) is the non-Brownian μ_{SAP}. The legends are identical to those in Fig. 7.13.

fluences of thermal fluctuations on the *flow* behaviors also suggests that the constants K_μ, K_ϕ, α_μ, and α_ϕ should be independent of the imposed pressure $\bar{\Pi}$. On the other hand, the arrest point (ϕ_m, μ_m) is affected by thermal fluctuations at low imposed pressure and approaches the SAP at high pressures. We use non-linear regression to simultaneously solve for the constants in Eq. (7.36) as well as the arrest points in Eq. (7.35) that best describe the rheological data in Fig. 7.13 for $I_v < 0.1$.

Fig. 7.18 presents the incremental volume fraction $\delta\phi$ and the incremental friction coefficient $\delta\mu$ as functions of the viscous number I_v from the non-linear regression

Table 7.1: The parameters for the model of glassy suspension rheology in Eq. (7.35)–(7.38) and Eq. (7.42).

K_μ	1.38	μ_G	0.021	$\bar{\Pi}_G$	3.5
α_μ	0.467	ϕ_G	0.603	c_m	0.168
K_ϕ	0.157	μ_{SAP}	0.13	β_y	0.552
α_ϕ	0.32	ϕ_{SAP}	0.652	K_d	0.037

for glassy suspensions with $\bar{\Pi} \geq 3.5$. The constants in Eq. (7.36) are given in Table 7.1. The results show impressive collapse of $\delta\phi$ and $\delta\mu$ at imposed pressures ranging from $\bar{\Pi} = 3.5$ to 1000. Moreover, for $I_v < 0.1$ the data follow the power law relation of Eq. (7.36), shown as dashed lines in Fig. 7.18. With $I_v > 0.1$, the incremental friction coefficient $\delta\mu$ becomes higher than the power relation at lower I_v, suggesting that Eq. (7.35) needs additional terms to captures the suspension behavior.

Fig. 7.18 demonstrates that the flow behavior of glassy suspensions can be described using Eq. (7.36) with constants K_μ, K_ϕ, α_μ, and α_ϕ independent of the imposed pressure $\bar{\Pi}$, and therefore confirms that the physics of jamming dominates the suspension dynamics. This is because the at-rest diffusive process in glassy suspensions, characterized by a diffusivity $d_T(\phi)$, is extremely slow as the particles are locked by their neighbors, i.e., $d_T(\phi)/d_0 \ll 1$. As a result, the suspension effective Péclet number $\text{Pe}_T = \dot{\gamma}a^2/d_T \gg 1$ for any finite strain rate $\dot{\gamma} > 0$, and therefore the suspension dynamics is always effectively in the non-Brownian limit and dominated by jamming.

The exponent $\alpha_\mu = 0.467$, that characterizes the behaviors of the incremental friction coefficient as $\delta\mu \sim I_v^{\alpha_\mu}$, is close to the experimental exponent of 0.5 [26]. This explains the good agreement between the shifted experimental data and the Brownian dynamics simulation results in Ref. [20]. Moreover, fitting the results from hydrodynamic simulations leads to $\alpha_\mu = 0.485$ [84], which is also close to the $\delta\mu$ behaviors here, suggesting weak influences of HIs. On the other hand, that the exponent $\alpha_\phi = 0.32$ that characterizes the volume fraction behaviors $\delta\phi \sim I_v^{\alpha_\phi}$ is 25% smaller than the exponent from hydrodynamic simulations [84], 0.40, suggests stronger influences of HIs.

The insets of Fig. 7.18 show the arrest volume fractions ϕ_m, in Fig. 7.18a, and the arrest friction coefficient μ_m, in Fig. 7.18b, as functions of the imposed pressure $\bar{\Pi}$. Both μ_m and ϕ_m increases with $\bar{\Pi}$ and approaches constant values corresponding

to the SAP. Since the imposed pressure is sufficiently high, we can directly identify the non-Brownian SAP $(\phi_{\mathrm{SAP}}, \mu_{\mathrm{SAP}}) = (0.652, 0.13)$. This is slightly different from the SAP in our previous study [20] due to the differences in the simulation protocol described in Sec. 7.2, and more importantly, the suspension rheology model. In Appendix 7.A we discuss the connection between the model here and the earlier universal viscosity divergence model [20]. Moreover, the arrest volume fractions ϕ_m and the imposed pressures Π are connected via

$$\bar{\Pi} = c_m/(\phi_{\mathrm{SAP}} - \phi_m), \tag{7.37}$$

where the constant c_m is shown in Table 7.1. Eq. (7.37) is a well-known relation for jammed packings [85], and arises from the diverging radial distribution function at contact near jamming. We also found that the μ_m and ϕ_m are well connected via

$$\frac{\mu_{\mathrm{SAP}} - \mu_m}{\mu_{\mathrm{SAP}} - \mu_G} = \left(\frac{\phi_{\mathrm{SAP}} - \phi_m}{\phi_{\mathrm{SAP}} - \phi_G}\right)^{\beta_y}, \tag{7.38}$$

where the constants β_y is also in Table 7.1, and the glass point $(\phi_G, \mu_G) = (0.603, 0.021)$ corresponds to the fitting results at the glassy pressure $\bar{\Pi}_G = 3.5$. The form of Eq. (7.38) also highlights the importance of the physics of jamming, as μ_m is determined as a distance from μ_{SAP} using the volume fraction distance from ϕ_{SAP}. Implicit to Eq. (7.38) is that the glassy state emerges abruptly as soon as the imposed pressure exceed $\bar{\Pi}_G$, and the arrest friction coefficient μ_m suddenly becomes finite. This critical behavior is consistent with the mode-coupling theory picture of the glass transition.

In Fig. 7.13, the yellow shaded area shows the glassy suspension boundary from Eq. (7.35)–(7.38) using the parameters in Table 7.1, and the dashed lines outline the glass limit $\bar{\Pi} = \bar{\Pi}_G$ and the jamming limit $\bar{\Pi} \to \infty$. Comparing to the simulations, the model appropriately outlines the glassy response ($\bar{\Pi} > 3.5$), and matches the simulation rheological outputs including η_s, ϕ, and μ with respect to I_v. However, the rheology model cannot follow the results for $I_v > 0.1$, especially for ϕ and μ, since more terms are required to capture the $\delta\phi$ and $\delta\mu$ behavior.

Fig. 7.19 presents the friction coefficient μ as a function of the volume fraction ϕ. The flow map is qualitatively similar to our earlier work [20]. The flowing suspension behaviors are divided to liquid-like and glassy, with the glassy suspensions near the flow-arrest transitions shown in yellow shaded region following the rheology model. Each symbol represents an isobar in the flow map. For liquid-like suspensions, the isobar becomes vertical and approaches the corresponding equilibrium fraction as

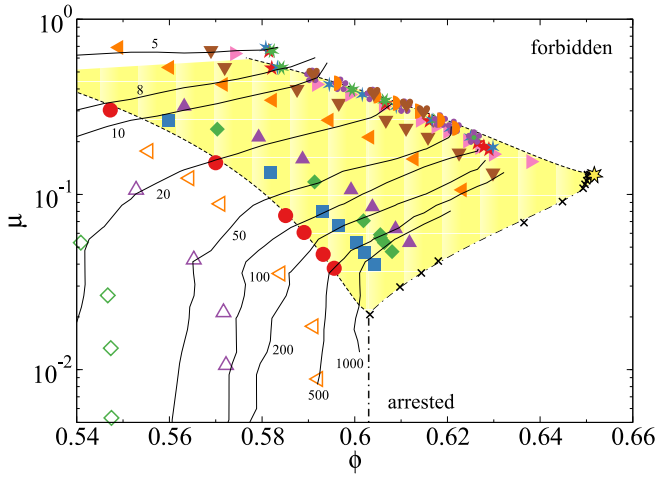

Figure 7.19: (Color online) The *macroscopic* friction coefficient $\mu = \sigma/\Pi$ as functions of the volume fraction ϕ for different imposed pressures $\bar{\Pi}$ for constant stress and pressure simulations. The legends are identical to Fig. 7.13. The shaded region bounded by the dashed lines are from the rheology model outlining the region of glassy behavior. The viscosity contours up to $\eta_s/\eta_0 = 10^3$ are shown in solid lines with annotated viscosity. The crosses show the arrest location (μ_m, ϕ_m) at different imposed pressure, and the dash-dotted line outlines the yield surface from Eq. (7.38). The Shear Arrest Point (SAP) is highlighted as a star at the intersection of the arrested, the forbidden, and the flowing region.

$\mu \to 0$. The glassy suspensions become flowing only if the imposed stress exceeds the yield stress. Therefore, an arrest region emerges at the lower half of Fig. 7.19. The volume fraction at the glassy pressure $\bar{\Pi}_G$ is $\phi_G = 0.603$, consistent with the mode-coupling glass transition point from the experiments on equilibrium colloidal suspensions with similar size polydispersity [22]. Further pressure increase leads to the collapsed non-Brownian behavior, and outlines a non-Brownian limiting behavior. A friction coefficient higher than non-Brownian limiting value is not physical for the given system. Consequently, a forbidden region emerges in the upper corner of the flow map. The intersection of the flowing, the forbidden, and the arrest region defines the SAP $(\phi_{\text{SAP}}, \mu_{\text{SAP}})$, the non-Brownian limit for sheared suspensions. The arrest points for the imposed pressures (ϕ_m, μ_m) are shown as crosses, and the model prediction from Eq. (7.38) is shown as a dash-dotted line. Note that at the glass transition density ϕ_G, our model assumes that the yield stress emerges abruptly.

Also presented in Fig. 7.19 are the suspension viscosity contours up to $\eta_s/\eta_0 = 10^3$. The qualitative features are identical our earlier work [20]. Without HIs, the

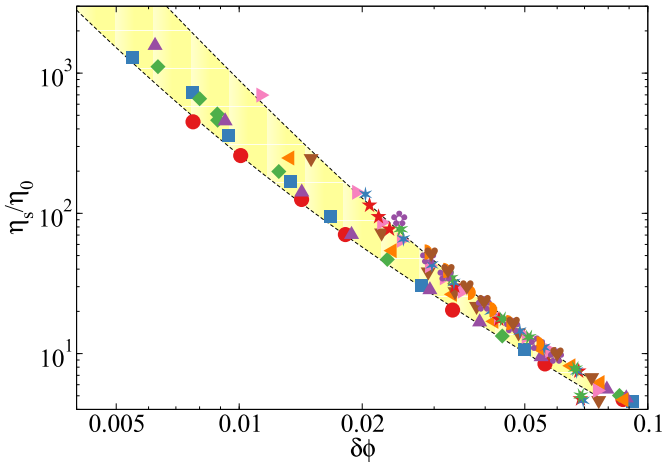

Figure 7.20: (Color online) The shear viscosity η_s/η_0 as a function of the volume fraction distance to the arrest $\delta\phi = (\phi_m - \phi)$ for glassy suspensions with $\bar{\Pi} \geq 3.5$. The yellow shaded region bounded by dashed lines are predictions from Eq. (7.39). The legends are identical to those in Fig. 7.13.

suspension viscosity at constant ϕ continues to decrease to a non-Brownian limiting value at all volume fractions. From linear response theory, the shear stress grows linearly with $\dot{\gamma}$, but the normal stress is increasing proportional to $\dot{\gamma}^2$. Therefore, it is always possible to find $\mu \ll 1$ such that the shear stress is non-zero but osmotic pressure changes little. Therefore, horizontally traversing the flow map in the limit of $\mu \to 0$ access the viscosity of equilibrium suspensions, and one approaches the viscosity divergence at ϕ_G differently from the constant pressure contours. Therefore, the viscosity divergence of equilibrium suspensions is expected to be different from the constant pressure viscosity divergence. Moreover, the rheology model does not describe the viscosity divergence of equilibrium suspensions near the glass transition since μ_m is finite. Near the boundary of the flow-arrest transitions, the viscosity contours are largely parallel to the arrest boundary shown as a dash-dotted line.

Fig. 7.20 explores the shear viscosity divergence of glassy suspensions as a function of the incremental volume fraction $\delta\phi$. The model in Sec. 7.5 shows that η_s changes with $\delta\phi$ as

$$\frac{\eta_s}{\eta_0} = \mu_m \left(\frac{\delta\phi}{K_\phi}\right)^{-\frac{1}{\alpha_\phi}} + K_\mu \left(\frac{\delta\phi}{K_\phi}\right)^{\frac{\alpha_\mu - 1}{\alpha_\phi}} . \tag{7.39}$$

The two-exponent divergence of the shear viscosity is evident in Fig. 7.20, and Eq. (7.39) with $\mu_m = \mu_G$ in the glass limit and $\mu_m = \mu_{\text{SAP}}$ in the jamming limit

describes the glassy suspensions results well in the yellow shaded region. Since μ_m changes from μ_G to μ_{SAP}, the viscosity divergence does not collapse to a universal curve presented in our earlier study [20]. In Appendix 7.A, we show that it is possible to shift the arrest volume fraction to $\hat{\phi}_m$ to recover the earlier universal viscosity divergence. Note that Fig. 7.18a shows the divergence of the normal viscosity $\eta_n \sim \delta\phi^{-1/\alpha_\phi}$, since the viscous number is the inverse normal viscosity, $I_v = \eta_0/\eta_n$.

An interesting corollary from the rheology model is that the strain rate Péclet number $\text{Pe}_{\dot{\gamma}} = \dot{\gamma}a^2/d_0$ at the non-Brownian limit SAP depends on how the SAP is approached. From Eq. (7.36) and (7.37), and the definition of I_v, the strain rate $\dot{\gamma} \sim \Pi(\delta\phi)^{1/\alpha_\phi} \sim \Delta_m^{-1}(\delta\phi)^{1/\alpha_\phi}$ where $\Delta_m = \phi_{\text{SAP}} - \phi_m$. The SAP is the double limit where $\delta\phi \to 0$ and $\Delta_m \to 0$, and the way the double limit is reached affects the value of $\dot{\gamma}$ at the SAP. For the general case of $\Delta_m \sim \delta\phi^p$ with $p > 0$, the strain rate at the SAP scales as $\dot{\gamma} \sim \text{Pe}_{\dot{\gamma}} \sim \delta\phi^{1/\alpha_\phi - p}$. Therefore, if $p > \alpha_\phi^{-1}$, approaching the SAP ($\delta\phi \to 0$) $\text{Pe}_{\dot{\gamma}} \to \infty$, the SAP corresponds to a true non-Brownian limit. If $p < \alpha_\phi^{-1}$, approaching the SAP leads to $\text{Pe}_{\dot{\gamma}} \to 0$. Here, the SAP corresponds to a vanishing $\text{Pe}_{\dot{\gamma}}$, suggesting that a non-Brownian limit with $\text{Pe}_{\dot{\gamma}} \to \infty$ does not exist [86]. Furthermore, when $p = \alpha_\phi^{-1}$, the strain rate Péclet number $\text{Pe}_{\dot{\gamma}}$ is finite at the SAP.

7.6 Connecting rheology, diffusion, and structure

Here we present the connections among the suspension rheology, diffusion, and structures beyond the granular perspective discussed in Sec. 7.5.

A diffusion-rheology flow map

To illustrate the connection between the suspension rheology and diffusion, Fig. 7.21 presents the stress scaled diffusivity d_∞^s/d_σ as functions of the inverse shear viscosity or the scaled strain rate, $\eta_0/\eta_s = \dot{\gamma}\eta_0/\sigma$, for different imposed pressures $\bar{\Pi}$. Scaling the diffusivity with d_σ in Eq. (7.30) leads to distinct behaviors for glassy and liquid-like suspensions. For liquid-like suspensions, the finite zero-shear viscosity and diffusivity lead to the divergence of d_∞^s/d_σ at finite η_0/η_s. Slightly increasing the stress does not significantly change the suspension viscosity, leading to rapid d_∞^s/d_σ reduction. Further stress increase causes the suspension viscosity to decrease due to suspension dilation and shear thinning. That d_∞^s/d_σ decreases with increasing η_0/η_s suggests that the diffusivity d_∞^s is not proportional to $\dot{\gamma}$, a relation commonly found in constant ϕ studies [51]. In the $\sigma \to \infty$ limit, $\phi \to 0$ due to dilation,

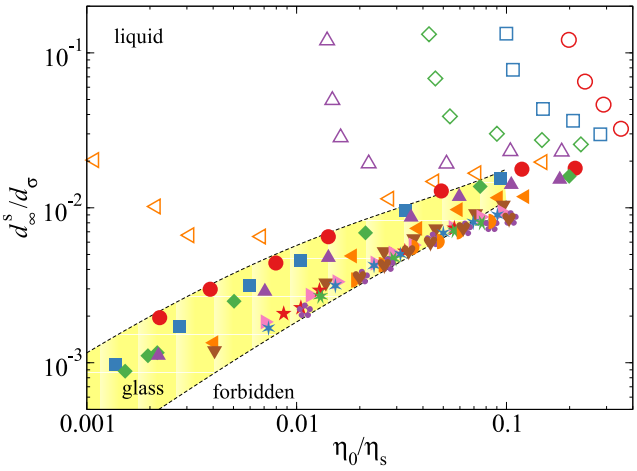

Figure 7.21: (Color online) The stress scaled long-time self-diffusivity in the vorticity direction, d^s_∞/d_σ, with the stress diffusion scale $d_\sigma = (a^2\sigma)/\eta_0$, as functions of the inverse viscosity $\eta_0/\eta_s = \dot{\gamma}\eta_0/\sigma$ over a wide range of imposed pressures $\bar{\Pi}$. The symbols are identical to those of Fig. 7.13. The shaded region bounded dash lines outlines the glassy suspension state from the model.

and therefore $\eta_0/\eta_s \to 1$. The stress-scaled diffusivity $d^s_\infty/d_\sigma \to 0$ as particles do not have neighbors to interact with and only move with the flow due to weak Brownian motions and low suspension volume fractions. However, this behavior can be disrupted by the string formation, which is excluded in Fig. 7.21.

With increasing Π, liquid-like suspensions begin to develop flow-arrest transitions. At $\bar{\Pi} = 3$, the stress-scaled diffusivity diverges at $\eta_0/\eta_s \approx 10^{-3}$. With increasing stress, d^s_∞/d_σ reaches a minimum, increases again to a maximum, and approaches zero as $\eta_0/\eta_s \to 1$. The growth of d^s_∞/d_σ with respect to η_0/η_s shows that the effect of flow overcomes the effect of dilation. With further increasing Π, the suspension enters the glass regime and d^s_∞/d_σ becomes qualitatively different. The divergence of d^s_∞/d_σ vanishes since, for glassy suspensions, the at-rest diffusivity approaches zero and the at-rest viscosity diverges. In Fig. 7.21, the stress-scaled diffusivity emerges from zero at $\eta_0/\eta_s \to 0$ for glassy suspensions. Further increase in Π slows down the growth of the stress-scaled diffusivity with respect to η_0/η_s, and the results begin to collapse as $\Pi \to \infty$, forming a jamming/granular limit. The suspension behavior beyond this limit is not physical regardless of the imposed stresses and pressures.

Fig. 7.21 highlights the distinct behaviors of liquid-like and glassy suspensions, and can be divided into the liquid-like region, the glass region, and the forbidden region.

Here, we present the glass region shaded yellow with dashed lines outlining the liquid-glass boundary and the jamming limit. As is demonstrated in Fig. 7.9b, for an imposed pressure, d^s_∞/d_σ depends only on the strain rate, and is not directly affected by the imposed stress σ. For constant strain rate rheology, Fig. 7.21 provides the connection between suspension mechanics and the dynamics. Moreover, the ratio of d^s_∞/d_σ to η_0/η_s is the strain rate scaled diffusivity $d^s_\infty/(a^2\dot\gamma)$. Fig. 7.21 shows that, for glassy suspensions, there is an upper limit of $d^s_\infty/(a^2\dot\gamma)$ taking place at the flow-arrest transition for each imposed pressure, and further increase in the stress reduces the diffusivity $d^s_\infty/(a^2\dot\gamma)$. Increasing Π reduces the maximum $d^s_\infty/(a^2\dot\gamma)$, and in the non-Brownian jamming limit ($\Pi \to \infty$), the at-rest diffusivity $d^s_\infty/(a^2\dot\gamma)$ reaches a minimum. In non-Brownian suspensions with hydrodynamic interactions, increasing flow also leads to decreasing scaled diffusivity $d^s_\infty/(a^2\dot\gamma)$ [87]. Clearly, this behavior does not originate from HIs.

Emerging Stokes-Einstein-Sutherland relation

To understand the suspension dynamics, comparing the time scale of particle diffusion, a^2/d^s_∞, to the time scale of flow, $\dot\gamma^{-1}$, defines a long-time Péclet number $\overline{\mathrm{Pe}}$,

$$\overline{\mathrm{Pe}} = \dot\gamma a^2/d^s_\infty. \tag{7.40}$$

The particle behaviors are driven by flow if $\overline{\mathrm{Pe}} \gg 1$ and by diffusion if $\overline{\mathrm{Pe}} \ll 1$. To account for particle interactions, we define the interaction friction coefficient

$$\mu^{\mathrm{I}} = \mu - (1 + \tfrac{5}{2}\phi)I_v, \tag{7.41}$$

which arises from the interparticle stress $\sigma^{\mathrm{I}} = \sigma - (1 + \frac{5}{2}\phi)\eta_0\dot\gamma$, and is identical to ${\sigma_{12}}^{\mathrm{P}}$ in Eq. (7.9) for systems without HIs. Accordingly, the interaction viscosity is defined as $\eta^{\mathrm{I}} = \mu^{\mathrm{I}}/I_v$. In the limit of vanishing flow, $I_v \to 0$, the interaction quantities approach the suspension quantities, $\mu^{\mathrm{I}} \to \mu$ and $\eta^{\mathrm{I}} \to \eta_s$.

Fig. 7.22a presents μ^{I} as a function of $\overline{\mathrm{Pe}}$ for a wide range of imposed pressures. Surprisingly, *all* the results for liquid-like and glassy suspensions collapse on to a single master curve, showing a universal connection between the suspension rheology and dynamics. Liquid-like suspensions can achieve both $\overline{\mathrm{Pe}} < 1$ and $\overline{\mathrm{Pe}} > 1$. For liquid-like suspensions, with weak imposed flow $\overline{\mathrm{Pe}} \ll 1$, the diffusion process is dominated by thermal fluctuations characterized by the zero-shear diffusivity. On the other hand, glassy suspensions can only reach $\overline{\mathrm{Pe}} \gtrsim 1$, showing that the diffusion process follows the imposed flow, as the at-rest diffusion is zero.

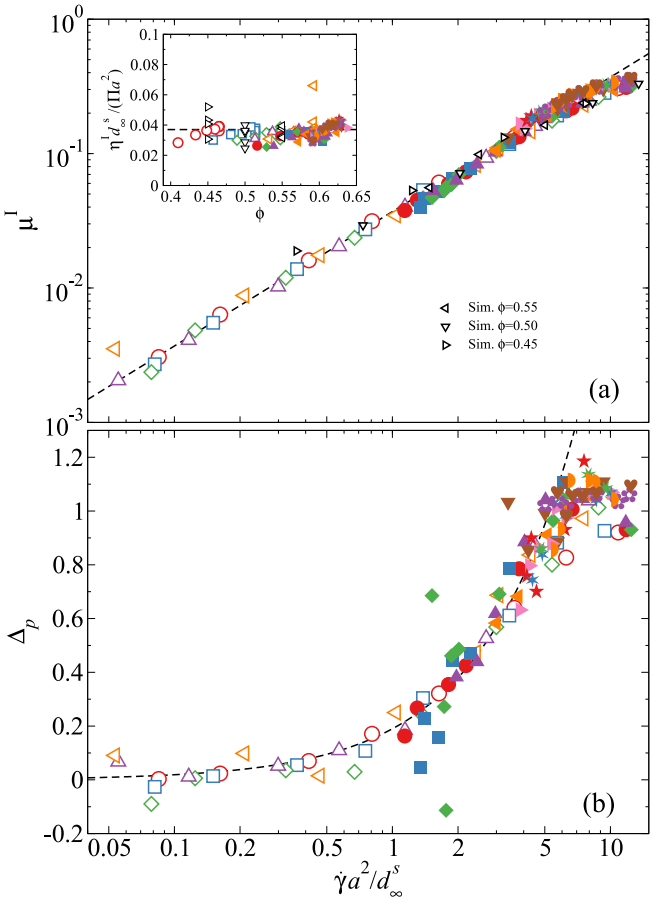

Figure 7.22: (Color online) (a) The interaction friction coefficient, $\mu^{\mathrm{I}} = \mu - (1 + \frac{5}{2}\phi)I_v$, as a function of the long-time Péclet number $\dot{\gamma}a^2/d^s_\infty = \overline{\mathrm{Pe}}$ over a wide range of imposed pressure $\bar{\Pi}$. The dashed line shows the linear relation of Eq. (7.42). The inset shows the scaled product $\eta^{\mathrm{I}} d^s_\infty/(\Pi a^2)$ as a function of the volume fraction ϕ, with the interaction viscosity $\eta^{\mathrm{I}} = \mu^{\mathrm{I}}/I_v$. Also presented are the constant volume Brownian Dynamics simulation results [51] at different ϕ. (b) The peak difference $\Delta_p = \max(g_{\mathrm{comp}}) - \max(g_{\mathrm{ext}})$ as a function of $\overline{\mathrm{Pe}}$. The dashed line represents the linear relation $\Delta_p = K_p\overline{\mathrm{Pe}}$ with $K_p = 0.19$. In (a) and (b), the symbols are identical to those of Fig. 7.13.

The following equation describes the data collapse in Fig. 7.22a for $\overline{\mathrm{Pe}} \lesssim 5$:

$$\mu^{\mathrm{I}} = K_d\overline{\mathrm{Pe}}, \tag{7.42}$$

where the constant $K_d = 0.037$. This is confirmed by the dashed line in Fig. 7.22. Rearranging Eq. (7.42) leads to

$$\eta^{\mathrm{I}} d^s_\infty/(\Pi a^2) = K_d. \tag{7.43}$$

The inset of Fig. 7.22a presents $\eta^{\mathrm{I}} d^s_\infty/\Pi$ as a function of the volume fraction ϕ. As expected, $\eta^{\mathrm{I}} d^s_\infty/\Pi \approx 0.037$ regardless of the volume fraction, the imposed stresses, and the confining pressures. Introducing an effective temperature $k_{\mathrm{B}}T_{\mathrm{eff}} = \Pi a^3$, Eq. (7.43) resembles an SES relation with T_{eff}. For $\overline{\mathrm{Pe}} \gtrsim 5$, the interaction friction coefficient μ^{I} becomes lower than the expected linear relation in Fig. 7.22. Here, the dynamics of flow become significantly faster than the diffusive dynamics. In this limit, the suspension begins to develop string phase structures that further suppresses the particle diffusion, leading to this deviation. Fig. 7.22a shows that the suspension pressure is a crucial aspect for modeling the dynamics of dense suspensions. Indeed, this is also apparent in Eq. (7.19) for weakly sheared suspensions, where the contact value $g^{\mathrm{eq}}(2)$ is proportional to the suspension pressure. Our results extend this insight to dense and strongly sheared suspensions.

In Fig. 7.22, for glassy suspensions $\overline{\mathrm{Pe}} \gtrsim 1$, and the minimum $\overline{\mathrm{Pe}}$ takes place in the limit of the glass transition. This is consistent with the highest slope of in the liquid-glass boundary in Fig. 7.21. With $\overline{\mathrm{Pe}} \approx 1$, the corresponding $\mu^{\mathrm{I}} \approx 0.03$, is slightly higher than the glass transition friction coefficient μ_G in Table 7.1. Therefore, as the suspension becomes glassy, it abruptly attains a finite yield stress, consistent with the glassy dynamics in the mode-coupling theory [4]. On the other hand, in the non-Brownian SAP, the limiting friction coefficient $\mu_{\mathrm{SAP}} \approx 0.13$ corresponds to $\overline{\mathrm{Pe}} \approx 4.2$ in Fig. 7.22a. Here, as the volume fraction reaches ϕ_{SAP}, the particle diffusivity also approaches its maximum. This is also consistent with the findings of Fig. 7.21, suggesting that for non-Brownian suspensions, particle diffusion arises from particle interactions, which reaches maximum in the jamming limit.

Fig. 7.22a also presents the constant volume and constant strain rate simulations of Foss and Brady [51] in triangles at different volume fractions. Despite small differences, the earlier results agree with the constant stress and pressure simulations. The differences most likely arise from the monodisperse systems used by Foss and Brady [51], which is more prone to structural developments at low and high strain rates comparing to polydisperse systems here. The agreement shows that data collapse in Fig. 7.22 is not specific to the constant stress and pressure rheology, and is general for hard-sphere suspensions.

The universal SES relation revealed in Fig. 7.22a is a new discovery on the rheology and dynamics of dense colloidal suspensions. For dense systems without shear, the SES relation is generally violated due to dynamic heterogeneity [43], with the notable exception of systems with ultra soft potentials [88, 89]. The results demonstrates

the critical role of the suspension pressure in particle diffusive dynamics, and confirms the idea that pressure sets the internal time scale of system [28]. More specifically, the suspension pressure can be considered an effective temperature $T_{\text{eff}} \propto \Pi$. Comparing to other definitions of the effective temperatures [45, 46, 90], $T_{\text{eff}} \propto \Pi$ is rather simple. However, it satisfies the fluctuation-dissipation relation (the SES relation), and in the dilute limit, $T_{\text{eff}} \to T$. Distinct from other studies, in this work the base state is the infinitely dilute suspension, suggesting that both the imposed flow and the presence of particles drive the system away from the base state.

Structure, diffusion, and rheology

In Fig. 7.22b we adopt the structural peak difference,

$$\Delta_p = \max(g_{\text{comp}}) - \max(g_{\text{ext}}), \tag{7.44}$$

to characterize how the suspension microstructure connects to its diffusive and rheological behavior. The peak difference Δ_p illustrates the suspension structural distortions, and approximates the structural contributions to the hard-sphere Brownian stresses in Eq. (7.19). Fig. 7.22b shows Δ_p as a function of the long-time Péclet number $\overline{\text{Pe}}$ over a wide range of confining pressures $\bar{\Pi}$. Despite some data scattering due to difficulties in measuring the suspension structures near the flow-arrest transition, the peak difference Δ_p also collapses with respect to $\overline{\text{Pe}}$, illustrating the structural changes are in concert with the suspension rheology and dynamics in a universal way.

When $\overline{\text{Pe}} \lesssim 5$, the peak difference Δ_p is linear in $\overline{\text{Pe}}$ as,

$$\Delta_p = K_p \overline{\text{Pe}}, \tag{7.45}$$

where $K_p \approx 0.19$, The linear relation is illustrated in dashed line in Fig. 7.22b. Therefore, the structural distortion is independent of Π for dense suspensions even close to the SAP. With $\mu^{\text{I}} \propto \overline{\text{Pe}}$ in Eq. (7.42), we reach a stress-structure relation,

$$\sigma^{\text{I}} = (K_d/K_p)\Pi\Delta_p, \tag{7.46}$$

suggesting that the shear stress is only related to the structural distortion and the suspension pressure, and is also consistent with the linear response results of Eq. (7.19). For liquid-like suspensions, Δ_p emerges from zero and grows linearly with $\overline{\text{Pe}}$, suggesting that the structural distortion emerges smoothly from isotropic equilibrium

suspensions. For glassy suspensions, however, because $\overline{\mathrm{Pe}} \gtrsim 1$, the structural distortion is present even at the flow-arrest transition. Therefore, the glassy suspension structures are inherently distorted, and the distortion grows with the flow. In the high pressure limit ($\bar{\Pi} \to \infty$), Δ_p is a minimum at the SAP. Clearly, structural distortion proceeds flow in dense suspensions. The finite structural distortion also suggests that the SAP is inherently anisotropic, and is distinct from the isotropic jammed state obtained from protocols such as rapid compression [63] or energy minimization [91].

At higher $\overline{\mathrm{Pe}}$, Δ_p becomes insensitive to $\overline{\mathrm{Pe}}$ and reaches a plateau. For the same $\overline{\mathrm{Pe}}$ range, Fig. 7.22a shows that μ^{I} deviates from the linear relation $\mu^{\mathrm{I}} \propto \overline{\mathrm{Pe}}$. These behaviors show, as expected, that the suspension structures are intimately related to the stresses. Further increasing $\overline{\mathrm{Pe}}$ leads to string phase formation, which further suppresses the particle diffusion and reduces the peak difference Δ_p. Therefore, $\overline{\mathrm{Pe}} \gtrsim 5$ implies that the suspension enters a new regime, where the suspension structures and rheology are less sensitive to $\overline{\mathrm{Pe}}$, preceding the order formation.

7.7 Summary and Conclusions

In this work, we studied the constant shear stress and pressure rheology of dense hard-sphere colloidal suspensions using Brownian Dynamics simulations without HIs. We particularly focused on the mechanical response, structural features, and diffusive dynamics of suspensions exhibiting flow-arrest transitions. Mechanically, comparing to constant volume rheology, fixing the confining pressure leads to dilation and stronger shear thinning in the shear and normal viscosities, η_s and η_n. With increasing confining pressure, the suspension changes from liquid-like to glassy, and flows only if the imposed stress exceeds the yield stress. Structurally, the suspension develops string phase at high imposed stress. For amorphous suspensions, the structural distortion increases with increasing stress. Dynamically, different characterizations of the suspension diffusion, including the long-time self-diffusivity d^s_∞, the wave-space diffusivity at the minimum wave number $D(q_{\min})$, the α-relaxation time τ_α near the first peak of the static structure factor, and the dynamic susceptibility χ_4, exhibit similar behaviors in the velocity gradient and the vorticity directions. The formation of a string phase qualitatively alters the suspension diffusive dynamics.

We analyzed the temporal and spatial dynamics of glassy suspensions near the flow-arrest transitions. By temporal coarse graining, we found that that the strain

rate distribution $P(\dot{\gamma})$ near the flow-arrest transition consists of a sharp peak in the arrested state and a broader peak at finite strain rate. Increasing the imposed stress eliminates the peak in the arrested state, and shifts $P(\dot{\gamma})$ towards a Gaussian. The stress-scaled diffusivity d^s_∞/d_σ is independent of σ and ϕ and is only directly controlled by the $\dot{\gamma}$ and Π. In addition, by analyzing particle trajectories, we found that the immediate neighbors of a *fast* particle are more likely to be fast, suggesting that the emergence of flow from an arrested state involves cooperative motions of fast particles in a dynamically heterogeneous fashion.

We characterized the suspension rheology using the viscosity number $I_v = \dot{\gamma}\eta_0/\Pi$, emphasizing the importance of pressure. In the limit of $\Pi \to \infty$, the suspension approaches the non-Brownian limit, and with vanishing I_v the friction coefficient reaches a minimum and the volume fraction reaches a maximum known as the SAP, $(\phi_{\text{SAP}}, \mu_{\text{SAP}})$ [20]. For normal stress differences, $N_1 > 0$ and $N_2 < 0$ for all imposed pressures. The suspension structural distortion, characterized by the peak values of the pair distribution function in the compressional and the extensional axes, $\max(g_{\text{comp}})$ and $\max(g_{\text{ext}})$, decreases with I_v and collapses in the $\Pi \to \infty$ limit. Moreover, suspension diffusion behaviors over different length scales show consistent behaviors, and reveal the non-Brownian high-pressure limiting behaviors when scaled with pressure.

We found that glassy suspensions begin to flow from an arrest point (ϕ_m, μ_m), which asymptotes the SAP in the $\Pi \to \infty$ limit. Away from the arrest point, the incremental friction coefficient $\delta\mu$ and the incremental volume fraction $\delta\phi$ change with the viscous number following power laws in Eq. (7.36), with the same constants for all pressures of glassy suspensions. The results show that the physics of jamming dominates the glassy suspension behavior, and thermal fluctuations only affect the arrest location. The results also show that the behavior of glassy suspensions can be succinctly summarized in a simple rheology model.

We discovered connections in the suspension structure, dynamics, and mechanics. We first constructed a diffusion-rheology map of the stress-scaled diffusivity and the inverse shear viscosity, with distinct liquid-like and glassy suspension behaviors. Since the stress-scaled diffusivity is only directly affected by Π and $\dot{\gamma}$, this flow map provides a direct connection between the suspension diffusion and rheology. We also found that the interaction friction coefficient μ^{I} as a function of $\dot{\gamma}a^2/d^s_\infty$ collapses for all imposed pressures and stresses, and that $\mu^{\text{I}} \propto \dot{\gamma}a^2/d^s_\infty$ when $\dot{\gamma}a^2/d^s_\infty \lesssim 5$. This leads to a non-equilibrium SES relation between η^{I} and d^s_∞

with an effective temperature proportional to the pressure, $T_{\text{eff}} \propto \Pi$. In addition, the suspension structural distortions, characterized by the peak difference Δ_p, also collapses as functions of $\dot{\gamma}a^2/d_\infty^s$, illustrating the close connection between the suspension structure and rheology.

This work is a comprehensive investigation of the constant stress and pressure rheology of dense colloidal suspensions. The results demonstrate the critical role of suspension pressure, and show that the granular perspective based on the viscous number is effective in connecting the behaviors of Brownian and non-Brownian suspensions. Our work also provides new perspectives in the mean-field modeling of colloidal suspensions using an effective temperatures proportional to the pressure. Moreover, the rheology and diffusion model is useful for predicting macroscopic suspension behaviors including particle migration and mixing in complex geometries and flow conditions [92].

7.A Universal viscosity divergences

The rheology of glassy suspensions in Sec. 7.5 can also be described using the universal divergence of the shear viscosity $\eta_s = \sigma/\dot{\gamma}$ and the incremental normal viscosity $\eta_n' = (\Pi - \Pi^{\text{eq}})/\dot{\gamma}$ in Eq. (7.1) with $\alpha = 2$ using a different set of arrest volume fractions $\hat{\phi}_m$. Fig. 7.23 presents η_s and η_n' as functions of the incremental volume fraction $\delta\hat{\phi} = \hat{\phi}_m - \phi$. With the new set of $\hat{\phi}_m$, both η_s and η_n' collapse and $\{\eta_s, \eta_n'\} \propto \delta\hat{\phi}^2$. The results are consistent with earlier findings [20]. The inset of Fig. 7.23 show the shift in $\hat{\phi}_m$ from the arrest volume fraction ϕ_m in Fig. 7.18a, $\Delta\phi = \hat{\phi}_m - \phi_m$ as a function of the imposed pressure $\bar{\Pi}$. The volume fraction difference $\Delta\phi$ in the glass limit, $\bar{\Pi} = \bar{\Pi}_G = 3.5$, is almost zero, and decreases to $\Delta\phi \approx -0.01$ in the $\Pi \to \infty$ limit, reducing the ϕ_{SAP} from 0.652 using models in Sec. 7.5 to 0.642 via Eq. (7.1), much closer to earlier results [20]. Clearly, the value of ϕ_{SAP} depends on the model selected to describe the data.

Moreover, the constants k_s and k_n in Eq. (7.1) can also be interpreted using the rheology model of Eq. (7.36), but the constant $K_\phi = K_\phi(\Pi)$ is also a function of the imposed pressure. Therefore, the universal viscosity divergence in Ref. [20] suggests that

$$k_s = \mu_m K_\phi^{\frac{1}{\alpha_\phi}} \quad \text{and} \quad k_n = \left(1 - \frac{\Pi^{\text{eq}}}{\Pi}\right) K_\phi^{\frac{1}{\alpha_\phi}} \tag{7.47}$$

are also constants. Note that at the flow-arrest transitions, the pressure is not the same as Π^{eq} since dilation precedes flow. The viscosity divergence description solely depends on the volume fraction behaviors and address changes in $\delta\mu$. Therefore,

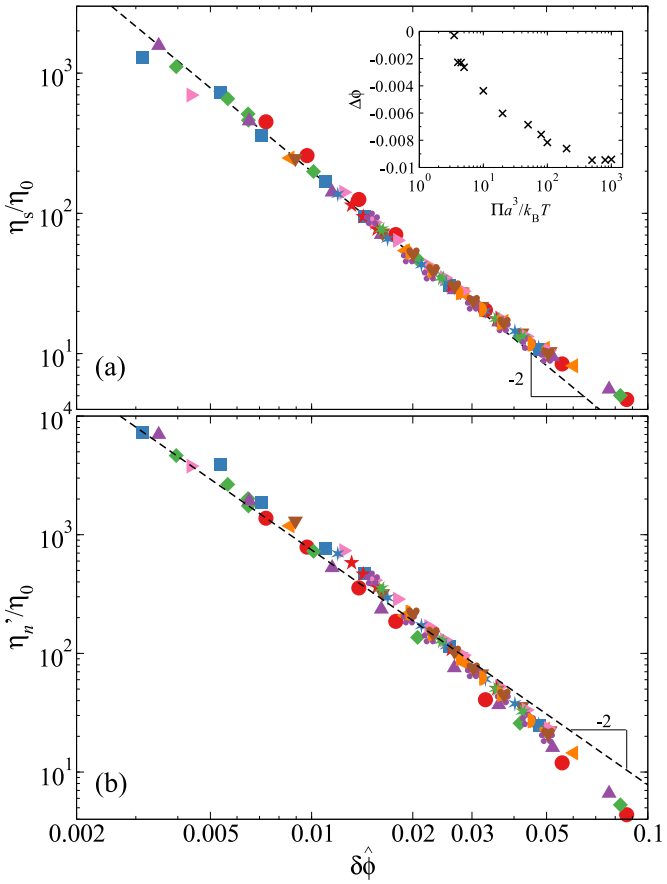

Figure 7.23: The shear viscosity η_s (a) and the incremental normal viscosity η_n' (b) as functions of the volume fraction distance from arrest $\delta\hat{\phi} = \hat{\phi}_m - \phi$. The dashed lines present the algebraic viscosity divergence $\{\eta_s, \eta_n'\} \propto \delta\hat{\phi}^2$. The inset shows the arrest volume fraction difference $\Delta\phi = \hat{\phi}_m - \phi_m$ as a function of the imposed pressure $\bar{\Pi}$, with ϕ_m from the inset of Fig. 7.18a. The legends are identical to those of Fig. 7.13.

despite the same physical interpretation of the suspension behaviors, the model in Sec. 7.5 have a wider range of applicability due to the additional descriptions on $\delta\mu$.

Another interpretation of Eq. (7.1) is based on the Herschel-Bulkley rheology of the pressure,

$$\Pi(\phi, \dot{\gamma}) = \Pi_m(\phi) + a(\phi)\dot{\gamma}^{\alpha_\gamma}, \tag{7.48}$$

and the existence of yield stress and pressure [93]. Expanding Eq. (7.48) at the flow-arrest transition with zero strain rate and the volume fraction ϕ_m to a flowing state with $(\phi, \dot{\gamma})$, we have

$$\Delta\Pi = -\partial\Pi/\partial\phi|_{(\phi_m,0)}\delta\phi + \partial\Pi/\partial(\dot{\gamma}^{\alpha_\gamma})|_{(\phi_m,0)}\dot{\gamma}^{\alpha_\gamma}. \tag{7.49}$$

Solving for $\dot{\gamma}$ in Eq. (7.49) with constant imposed pressure, $\Delta\Pi = 0$, leads to $\dot{\gamma} \propto \delta\phi^{1/\alpha_\gamma}$. Therefore, with finite yield stress σ_m and yield pressure difference $(\Pi_m - \Pi^{eq})$, Eq. (7.48) suggests the viscosities $\{\eta_s, \eta_n'\} \propto \delta\phi^{1/\alpha_\gamma}$. Note that $\Pi_m(\phi) > \Pi^{eq}(\phi)$ because dilation precedes flow in glassy suspensions. With $\alpha_\gamma = 0.5$, this interpretation connects our works to earlier constant volume studies with soft particle systems [21, 25, 32]. However, this interpretation also ignores changes in $\delta\mu$ and suffers similar limitations as Eq. (7.47).

References

[1] W. B. Russel, D. A. Saville, and W. R. Schowalter, *Colloidal dispersions* (Cambridge University Press, 1991).

[2] R. J. Hunter, *Foundations of colloid science* (Oxford University Press, 2001).

[3] P. N. Pusey and W. van Megen, "Phase behaviour of concentrated suspensions of nearly hard colloidal spheres", Nature **320**, 340 (1986).

[4] W. Götze, *Complex dynamics of glass-forming liquids: a mode-coupling theory* (Oxford University Press, 2008).

[5] G. L. Hunter and E. R. Weeks, "The physics of the colloidal glass transition", Rep. Prog. Phys. **75**, 066501 (2012).

[6] N. Koumakis, M. Laurati, S. U. Egelhaaf, J. F. Brady, and G. Petekidis, "Yielding of hard-sphere glasses during start-up shear", Phys. Rev. Lett. **108**, 098303 (2012).

[7] M. Ballauff, J. M. Brader, S. U. Egelhaaf, M. Fuchs, J. Horbach, N. Koumakis, M. Krüger, M. Laurati, K. J. Mutch, G. Petekidis, M. Siebenbürger, T. Voigtmann, and J. Zausch, "Residual stresses in glasses", Phys. Rev. Lett. **110**, 215701 (2013).

[8] H. M. Laun, "Rheological properties of aqueous polymer dispersions", Angewandte Makromolekulare Chemie **123/124**, 335 (1984).

[9] X. Cheng, J. H. McCoy, J. N. Israelachvili, and I. Cohen, "Imaging the microscopic structure of shear thinning and thickening colloidal suspensions", Science **333**, 1276 (2011).

[10] N. J. Wagner and J. F. Brady, "Shear thickening in colloidal dispersions", Phys. Today **62**, 27 (2009).

[11] C. D. Cwalina and N. J. Wagner, "Material properties of the shear-thickened state in concentrated near hard-sphere colloidal dispersions", J. Rheol. **58**, 949 (2014).

[12] J. Mewis and N. J. Wagner, *Colloidal suspension rheology* (Cambridge University Press, 2013).

[13] S. Torquato and F. H. Stillinger, "Jammed hard-particle packings: from kepler to bernal and beyond", Rev. Mod. Phys. **82**, 2633 (2010).

[14] A. J. Liu and S. R. Nagel, "Nonlinear dynamics: jamming is not just cool any more", Nature **396**, 21 (1998).

[15] L. Berthier and G. Biroli, "Theoretical perspective on the glass transition and amorphous materials", Rev. Mod. Phys. **83**, 587 (2011).

[16] A. J. Liu and S. R. Nagel, "The jamming transition and the marginally jammed solid", Annu. Rev. Condens. Matter Phys. **1**, 347 (2010).

[17] Y. Forterre and O. Pouliquen, "Flows of dense granular media", Annu. Rev. Fluid Mech. **40**, 1 (2008).

[18] M. Rubinstein and R. H. Colby, *Polymer physics* (Oxford University Press, 2003).

[19] P. Guan, M. Chen, and T. Egami, "Stress-temperature scaling for steady-state flow in metallic glasses", Phys. Rev. Lett. **104**, 205701 (2010).

[20] M. Wang and J. F. Brady, "Constant stress and pressure rheology of colloidal suspensions", Phys. Rev. Lett. **115**, 158301 (2015).

[21] A. Ikeda, L. Berthier, and P. Sollich, "Unified study of glass and jamming rheolgy in soft particle systems", Phys. Rev. Lett. **109**, 018301 (2012).

[22] G. Brambilla, D. El Masri, M. Pierno, L. Berthier, L. Cipelletti, G. Petekidis, and A. Schofield, "Probing the equilibrium dynamics of colloidal hard spheres above the mode-coupling glass transition", Phys. Rev. Lett. **102**, 085703 (2009).

[23] W. van Megen, T. C. Mortensen, S. R. Williams, and J. Müller, "Measurement of the self-intermediate scattering function of suspensions of hard spherical particles near the glass transition", Phys. Rev. E **58**, 6073 (1998).

[24] J. Reinhardt, F. Weysser, and M. Fuchs, "Comment on "probing the equilibrium dynamics of colloidal hard spheres above the mode-coupling glass transition"", Phys. Rev. Lett. **105**, 199604 (2010).

[25] A. Ikeda, L. Berthier, and P. Sollich, "Disentangling glass and jamming physics in the rheology of soft materials", Soft Matter **9**, 7669 (2013).

[26] F. Boyer, E. Guazzelli, and O. Pouliquen, "Unifying suspension and granular rheology", Phys. Rev. Lett. **107**, 188301 (2011).

[27] W. B. Russel, N. J. Wagner, and J. Mewis, "Divergence in the low shear viscosity for brownian hard sphere dispersions: at random close packing or the glass transition?", J. Rheo. **57**, 1555 (2013).

[28] P. Jop, Y. Forterre, and O. Pouliquen, "A constitutive law for dense granular flows", Nature **441**, 727 (2006).

[29] M. Trulsson, B. Andreotti, and P. Claudin, "Transition from the viscous to inertial regime in dense suspensions", Phys. Rev. Lett. **109**, 118305 (2012).

[30] E. Lerner, G. Düring, and M. Wyart, "A unified framework for non-brownian suspension flows and soft amorphous solids", Proc. Natl. Acad. Sci. U.S.A. **109**, 4798 (2012).

[31] E. DeGiuli, G. Düring, E. Lerner, and M. Wyart, "Unified theory of inertial granular flows and non-brownian suspensions", Phys. Rev. E **91**, 062206 (2015).

[32] T. Kawasaki, D. Coslovich, A. Ikeda, and L. Berthier, "Diverging viscosity and soft granular rheology in non-brownian suspensions", Phys. Rev. E **91**, 012203 (2015).

[33] J. K. G. Dhont, *An introduction to dynamics of colloids* (Elsevier, Amsterdam, 1996).

[34] A. J. Banchio and G. Nägele, "Short-time transport properties in dense suspensions: from neutral to charge-stabilized colloidal spheres", J. Chem. Phys. **128**, 104903 (2008).

[35] A. M. Leshansky and J. F. Brady, "Dynamic structure factor study of diffusion in strongly sheared suspensions", J. Fluid Mech. **527**, 141 (2005).

[36] A. M. Leshansky, J. F. Morris, and J. F. Brady, "Collective diffusion in sheared colloidal suspensions", J. Fluid Mech. **597**, 305 (2008).

[37] C. Toninelli, M. Wyart, L. Berthier, G. Biroli, and J.-P. Bouchaud, "Dynamical susceptibility of glass formers: contrasting the predictions of theoretical scenarios", Phys. Rev. E **71**, 041505 (2005).

[38] D. Lootens, H. Van Damme, and P. Hebraud, "Giant stress fluctuations at the jamming transition", Phys. Rev. Lett. **90**, 178301 (2003).

[39] C. Heussinger, L. Berthier, and J.-L. Barrat, "Superdiffusive, heterogeneous, and collective particle motion near the fluid-solid transition in athermal disordered materials", Europhys. Lett. **90**, 20005 (2010).

[40] C. Heussinger, P. Chaudhuri, and J.-L. Barrat, "Fluctuations and correlations during the shear flow of elastic particles near the jamming transition", Soft Matter **6**, 3050 (2010).

[41] A. Einstein, "Eine neue bestimmung der moleküldimensionen", Annalen der Physik **19**, 289 (1906).

[42] J. H. Simpson and H. Y. Carr, "Diffusion and nuclear spin relaxation in water", Phys. Rev. **111**, 1201 (1958).

[43] S. Kumar, G. Szamel, and J. F. Douglas, "Nature of the breakdown in the stokes-einstein relarelation in a hard sphere fluid", J. Chem. Phys. **124**, 214501 (2006).

[44] M. C. Miguel and J. M. Rubi, eds., *Jamming, yielding, and irreversible deformation in condensed matter* (Springer, 2006).

[45] L. F. Cugliandolo, "The effective temperature", J. Phys. A: Math. Theor. **44**, 483001 (2011).

[46] T. K. Haxton, "Ratio of effective temperature to pressure controls the mobility of sheared hard spheres", Physical Review E **85**, 011503 (2012).

[47] J. F. Brady, A. S. Khair, and M. Swaroop, "On the bulk viscosity of suspensions", J. Fluid Mech. **554**, 109 (2006).

[48] H. Goldstein, C. P. Poole Jr., and J. L. Safko, *Classical mechanics* (Addison-Wesley, 2001).

[49] D. M. Heyes and J. R. Melrose, "Brownian dynamics simulations of model hard-sphere suspensions", J. Non-Newtonian Fluid Mech. **46**, 1 (1993).

[50] W. Schaertl and H. Sillescu, "Brownian dynamics simulations of colloidal hard spheres. effects of sample dimensionality on self-diffusion", J. Stat. Phys. **74**, 687 (1994).

[51] D. R. Foss and J. F. Brady, "Brownian dynamics simulation of hard-sphere colloidal dispersions", J. Rheol. **44**, 629 (2000).

[52] P. Strating, "Brownian dynamics simulation of a hard-sphere suspension", Phys. Rev. E **59**, 2175 (1999).

[53] M. Laurati, K. J. Mutch, N. Koumakis, J. Zausch, C. P. Amann, A. B. Schofield, G. Petekidis, J. F. Brady, J. Horbach, M. Fuchs, and S. U. Egelhaaf, "Transient dynamics in dense colloidal suspensions under shear: shear rate dependence", J. Phys.: Condens. Matter **24**, 464104 (2012).

[54] N. Koumakis, J. F. Brady, and G. Petekidis, "Complex oscillatory yeilding of model hard-sphere glasses", Phys. Rev. Lett. **110**, 178301 (2013).

[55] I. C. Carpen and J. F. Brady, "Microrheology of colloidal dispersions by brownian dynamics simulations", J. Rheo. **49**, 1483 (2005).

[56] R. N. Zia and J. F. Brady, "Stress development, relaxation, and memory in colloidal dispersions: transient nonlinear microrheology", J. Rheo. **57**, 457 (2013).

[57] U. M. Córdova-Figueroa and J. F. Brady, "Osmotic propulsion: the osmotic motor", Phys. Rev. Lett. **100**, 158303 (2008).

[58] S. C. Takatori, W. Yan, and J. F. Brady, "Swim pressure: stress generation in active matter", Phys. Rev. Lett. **113**, 028103 (2014).

[59] B. Lander, U. Seifert, and T. Speck, "Mobility and diffusion of a tagged particle in a driven colloidal suspension", Europhys. Lett. **92**, 58001 (2010).

[60] H. Jin, K. Kang, K. H. Ahn, and J. K. G. Dhont, "Flow instability due to coupling of shear-gradients with concentration: non-uniform flow of (hard-sphere) glasses", Soft Matter **10**, 9470 (2014).

[61] D. M. Heyes and H. Sigurgeirsson, "The newtonian viscosity of concentrated stabilized dispersions: comparisons with the hard sphere fluid", J. Rheo. **48**, 223 (2004).

[62] J. W. Swan and J. F. Brady, "Colloidal dispersions deformed by a steady shear stress", Submitted (2013).

[63] B. D. Lubachevsky and F. H. Stillinger, "Geometric properties of random disk packings", J. Stat. Phys. **60**, 561 (1990).

[64] M. Skoge, A. Donev, F. H. Stillinger, and S. Torquato, "Packing hyperspheres in high-dimensional Euclidean spaces", Phys. Rev. E **74**, 041127 (2006).

[65] J. F. Brady and J. F. Morris, "Microstructure of strongly sheared suspensions and its impact on rheology and diffusion", J. Fluid Mech. **348**, 103 (1997).

[66] J. F. Brady, "The rheological behavior of concentrated colloidal dispersions", J. Chem. Phys. **99**, 567 (1993).

[67] A. K. Gurnon and N. J. Wagner, "Microstructure and rheology relationships for shear thickening colloidal dispersions", J. Fluid Mech. **769**, 242 (2015).

[68] F. Westermeier, D. Pennicard, H. Hirsemann, U. H. Wagner, C. Rau, H. Graafsma, P. Schall, M. P. Lettinga, and B. Struth, "Connecting structure, dynamics and viscosity in sheared soft colloidal liquids: a medley of anisotropic fluctuations", Soft Matter **12**, 171 (2016).

[69] G. Nägele, "On the dynamics and structure of charge-stabilized suspensions", Phys. Rep. **272**, 215 (1996).

[70] M. Wang, M. Heinen, and J. F. Brady, "Short-time diffusion in concentrated bidisperse hard-sphere suspensions", J. Chem. Phys. **142**, 064905 (2015).

[71] M. Wang and J. F. Brady, "Short-time transport properties of bidisperse suspensions and porous media: a stokesian dynamics study", J. Chem. Phys. **142**, 094901 (2015).

[72] G. Nägele, J. Bergenholtz, and J. K. G. Dhont, "Cooperative diffusion in colloidal mixtures", J. Chem. Phys. **110**, 7037 (1999).

[73] D. El Masri, G. Brambilla, M. Pierno, G. Petekidis, A. Schofield, L. Berthier, and L. Cipelletti, "Dynamic light scattering measurements in the activated regime of dense colloidal hard spheres", J. Stat. Mech. Theor. Exp. **2009**, P07015 (2009).

[74] R. Zwanzig, *Nonequilibrium statistical mechanics* (Oxford University Press, 2001).

[75] E. R. Weeks, J. C. Crocker, A. C. Levitt, A. Schofield, and D. A. Weitz, "Three-dimensional direct imaging of structural relaxation near the colloidal glass transition", Science **287**, 627 (2000).

[76] A. Rahman, "Correlations in the motion of atoms in liquid argon", Phys. Rev. A **136**, 405 (1964).

[77] B. Gärtner, "Fast and robust smallest enclosing balls", in Proceedings of the 7th annual european symposium on algorithms (1999), p. 325.

[78] G. Biroli and J. P. Garrahan, "Perspective: the glass transition", J. Chem. Phys. **138**, 12A301 (2013).

[79] L. Berthier, G. Biroli, L. Bouchaud J.-P.and Cipelletti, and W. van Saarloos, eds., *Dynamical heterogeneities in glasses, colloids, and granular media* (Oxford University Press, 2011).

[80] C. H. Rycroft, "Voro++: a three-dimensional voronoi cell library in c++", Chaos **19**, 041111 (2009).

[81] J. F. Brady and M. Vivic, "Normal ststress in colloidal dispersions", J. Rheol. **39**, 545 (1995).

[82] J. Bergenholtz, J. F. Brady, and M. Vivic, "The non-newtonian rheology of dilute colloidal suspensions", J. Fluid Mech. **456**, 239 (2002).

[83] S. Torquato, *Random heterogeneous materials microstructure and macroscopic properties* (Springer, 2002).

[84] M. Wang and J. F. Brady, "Constant stress and pressure rheology of colloidal suspensions: the effects of hydrodynamic interactions", In Preparation (2016).

[85] M. D. Rintoul and S. Torquato, "Metastability and crystallization in hard-sphere systems", Phys. Rev. Lett. **77**, 4198 (1996).

[86] M. Wang and J. F. Brady, "Wang and brady reply", Phys. Rev. Lett. **116**, 179802 (2016).

[87] A. Sierou and J. F. Brady, "Shear-induced self-diffusion in non-colloidal suspensions", J. Fluid Mech. **506**, 285 (2004).

[88] A. Ikeda and K. Miyazaki, "Glass transition of the monodisperse gaussian core model", Phys. Rev. Lett. **106**, 015701 (2011).

[89] A. Ikeda and K. Miyazaki, "Slow dynamics of the high density Gaussian core model", J. Chem. Phys. **135**, 054901 (2011).

[90] T. K. Haxton and A. J. Liu, "Activated dynamics and effective temperature in a steady state sheared glass", Phys. Rev. Lett. **99**, 195701 (2007).

[91] C. S. O'Hern, L. E. Silbert, A. J. Liu, and S. R. Nagel, "Jamming at zero temperature and zero applied stress: the epitome of disorder", Phys. Rev. E **68**, 011306 (2003).

[92] T. Dbouk, E. Lemaire, L. Lobry, and F. Moukalled, “Shear-induced particle migration: predictions from experimental evaluation of the particle stress tensor”, J. Non-Newtonian Fluid Mech. **198**, 78 (2013).

[93] A. Ikeda, L. Berthier, and P. Sollich, “Comment on "constant stress and pressure rheology of colloidal suspensions””, Phys. Rev. Lett **116**, 179801 (2016).